PHYSICAL REVIEW D VOLUME 21, NUMBER 1 1 JANUARY 1980

Studies in the BNL 21-GeV/*c* negative-hyperon beam. II. Leptonic decays of Ξ and Σ

J. A. Thompson, W. E. Cleland, W. E. Cooper, M. Dris,* E. Engels, Jr., M. L. Herbert,† and D. E. Kraus
University of Pittsburgh, Pittsburgh, Pennsylvania 15260

D. Lowenstein
Brookhaven National Laboratory, Upton, New York 11973

(Received 10 July 1979)

The decays $\Sigma^- \to \Lambda e^- \nu$ and $\Xi^- \to \Lambda e^- \nu$ are studied in a counter–spark-chamber experiment using unpolarized hyperons from the BNL hyperon beam. A threshold Čerenkov counter identifies the electron. From a sample of 119 reconstructed $\Sigma^- \to \Lambda e^- \nu$ events (including ~ 5 background events), we find $(\Sigma^- \to \Lambda e^- \nu)/(\Sigma^- \to n\pi) = (0.63 \pm 0.10) \times 10^{-4}$ and $g_V/g_A = -0.32 \pm 0.30$, $g_{\rm WM} = -0.6 \pm 3.6$ (with sign convention of the Particle Data Group tables). We find ${\rm Im}(g_V/g_A) = 0.2 \pm 0.7$, consistent with time-reversal invariance. From a sample of 14 $\Xi^- \to \Lambda e^- \nu$ events (including ≈ 3.4 background events) we find $(\Xi^- \to \Lambda e^- \nu)/(\Xi^- \to \Lambda\pi) = (0.30 \pm 0.14) \times 10^{-3}$. We also searched for $\Xi^- \to \Lambda\mu\nu$ and $\Xi^- \to \Sigma^0 e\nu$ and set upper limits on these decays from our data.

I. INTRODUCTION

In this paper, the second (II) of a two-part series describing experiments in the BNL hyperon beam, we describe the results of our study of and search for leptonic decay modes of Σ and Ξ hyperons with a visible $\Lambda \to p\pi$ decay in the final state. In I (Ref. 1) we describe the details of our apparatus and analysis as related to results on the normal $\Sigma^- \to n\pi$ and $\Xi^- \to \Lambda\pi$ modes. In II we describe the apparatus, analysis, and results pertaining to the rare leptonic decays.

To describe the decay $A \to Bl\nu$, we use the matrix element $GL_\mu J_\mu$, where

$$L_\mu = \frac{\langle e|\gamma_\mu(1+\gamma_5)|\nu\rangle}{\sqrt{2}}\,,$$

$$J_\mu = \langle B|J_{\mu\ \rm vector}(q^2) + J_{\mu\ \rm axial}(q^2)|A\rangle\,,$$

and $q = P_A - P_B$ (four-vector). In this analysis we take $q^2 = 0$ in the form-factor expansion, and set second-class currents $= 0$, keeping only vector $g_V\gamma_\mu$, axial-vector $g_A\gamma_\mu\gamma_5$, and tensor or weak magnetism $g_{\rm WM}\sigma_{\mu\nu}q_\nu/m_A$ terms.

We then have

$$J_\mu = \left\langle B \left| g_V\gamma_\mu + \frac{g_{\rm WM}}{m_A}\sigma_{\mu\nu}q_\nu + g_A\gamma_\mu\gamma_5 \right| A \right\rangle .$$

Our sign convention is that of Refs. 2, 3, and 4 and opposite to that of Refs. 5, 6, and 7; in our sign convention g_A/g_V for $n \to pe\nu$ is positive. The Cabibbo theory[8] predicts that

$$J_\mu = J_\mu(\Delta S = 0)\cos\theta_{\rm Cab} + J_\mu(\Delta S = 1)\sin\theta_{\rm Cab}\,.$$

Thus the g_V, $g_{\rm WM}$, and g_A shown in the matrix element above will include a factor of $\cos\theta_{\rm Cab}$ for $\Sigma^- \to \Lambda e^-\nu$ and $\sin\theta_{\rm Cab}$ for $\Xi^- \to \Lambda e^-\nu$. Since $\theta_{\rm Cab}$ is expected to be of order 0.23 from previous measurements or from the phenomenological results of some models,[7-11] $\Sigma^- \to \Lambda e^-\nu$ is not sensitive to $\theta_{\rm Cab}$, but $\Xi^- \to \Lambda e^-\nu$, as a strangeness-changing decay, is. The form factors g_V and g_A are predicted for all hyperon leptonic decays from the Cabibbo theory, and are shown for some cases of interest in Table I. Once g_V and g_A are known, the matrix element can be integrated and the resulting rate can be combined with the known particle lifetime to give a predicted branching ratio. A useful compilation of the integrals of the phase-space parts of the matrix elements, (i.e., $\langle B|\gamma_\mu|A\rangle$, etc.) is given by Ref. 12. g_V is predicted to be zero for $\Sigma^- \to \Lambda e^-\nu$ decay from the strong conserved-vector-current (CVC) assumption, since an isospin-raising or -lowering operator will not connect the Σ and the Λ states. Also, from CVC and SU_3 arguments $g_{\rm WM}/g_A$ for $\Sigma^- \to \Lambda e^-\nu$ decay is predicted to be 1.7–2.0.[13-16]

For the $\Sigma^- \to \Lambda e^-\nu$ and $\Xi^- \to \Lambda e^-\nu$ studies the data from runs B and C, discussed in I were used. Our sample of $\Sigma^- \to \Lambda e^-\nu$ (119 candidates with 5 expected background events) is larger than the world sample that has been used for determining the branching ratio[17-20] and larger than that of any other single experiment used in determining the g_V/g_A ratio.[17-20] Systematic errors ($\approx 14\%$) are comparable to statistical errors (9.6%) for the $\Sigma^- \to \Lambda e^-\nu$ branching-ratio measurement, but statistical errors dominate in the $\Sigma^- \to \Lambda e^-\nu$ g_V/g_A, $g_{\rm WM}/g_A$ measurements.

Our sample of $\Xi^- \to \Lambda e^-\nu$ (14 events, with 3.4 expected background, including 1 possible event from the process $\Xi \to \Sigma^0 e\nu$) is larger than the world sample from experiments[21-28] in which $\Xi^- \to \Lambda e^-\nu$ and $\Xi^- \to \Sigma^0 e\nu$ have been separated. Because of the large background and few events we do not attempt a fit to g_A/g_V but present our

TABLE I. Cabibbo prediction for matrix-element forms.

Transition	$\langle B\|V\|A\rangle$	$\langle B\|A\|A\rangle$
$n \rightarrow p$	$\cos\theta_C$	$(D+F)\cos\theta_C$
$\Sigma \rightarrow \Lambda$	0	$(\frac{2}{3})^{1/2} D\cos\theta_C$
$\Xi \rightarrow \Lambda$	$(\frac{3}{2})^{1/2}\sin\theta_C$	$(\frac{3}{2})^{1/2}(F-D/3)\sin\theta_C$
$\Xi \rightarrow \Sigma$	$(\frac{1}{2})^{1/2}\sin\theta_C$	$(\frac{1}{2})^{1/2}(F+D)\sin\theta_C$

experimentally measured Dalitz plot, together with that expected for the background events and for the Cabibbo prediction for $\Xi^- \rightarrow \Lambda e^-\nu$. The error on our results for $\Xi^- \rightarrow \Lambda e^-\nu$ is dominated by the small statistics of our observed sample.

Our search for $\Xi^- \rightarrow \Sigma^0 e\nu$ lowers the upper limit[27] for the decay by a factor of 3, to approximately the Cabibbo prediction. Our search for $\Xi^- \rightarrow \Lambda\mu\nu$ lowers the observed branching ratio[27] by 30%, in the direction expected from phase-space arguments and the Cabibbo prediction.

Within our errors, we find no disagreements with Cabibbo-theory predictions. In our study of each decay mode we have the benefit of a large data sample and of the $\Xi^- \rightarrow \Lambda\pi$ normal-decay calibration studies described in paper I.

II. APPARATUS AND EXPERIMENTAL DETAILS PECULIAR TO THE β-DECAY MODES

A. Čerenkov counter

1. Construction and alignment

The incident beam and the Ξ, Σ, and Λ decay products were measured by a spectrometer system (Fig. 1) described in detail in I. An air Čerenkov counter ($\check{C}E$, Fig. 2) located inside the first magnet in the two-magnet spectrometer tagged electrons. This location ensures a large solid angle for the low-momentum electrons expected from $\Sigma^- \rightarrow \Lambda e^-\nu$ and $\Xi^- \rightarrow \Lambda e^-\nu$. Thus we achieved good detection efficiency over the Dalitz plot, but at the cost of a spread in the effective source of the photons because of the bending of the electrons in the magnet. We have checked, as described below, that light-collection variations introduce no efficiency variations over the Dalitz plot, to within our statistics.

The counter had four mirrors constructed from 0.4 cm lucite. Their dimensions were 30 cm × 60 cm with radius of curvature about 125 cm. The two left mirrors directed light to one phototube (CL), and the two right mirrors directed light onto the other phototube (CR). The tubes were 12.6-cm RCA 8854, having a gallium-phosphide first dynode, which gives high electron multiplica-

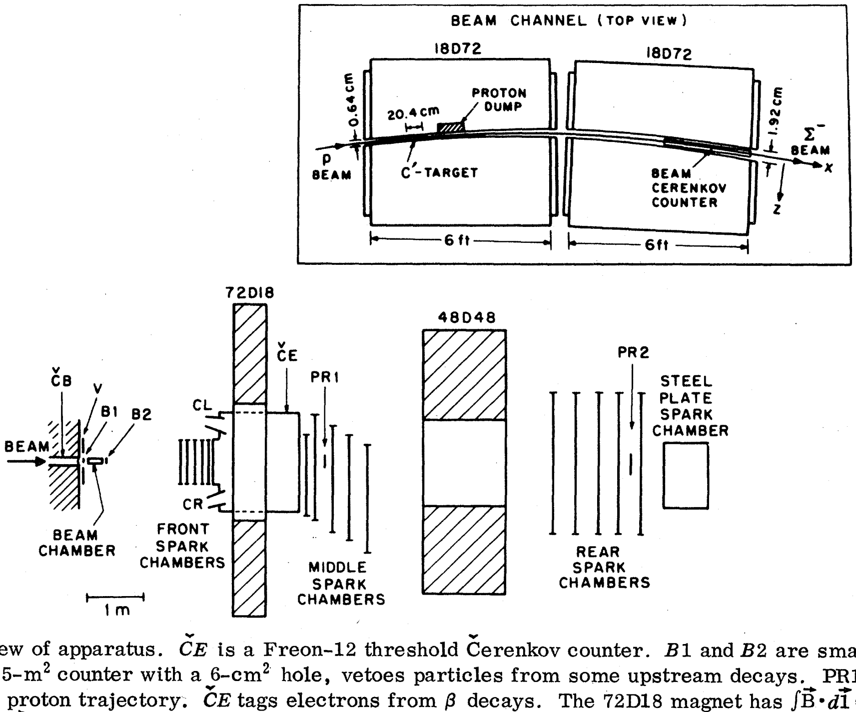

FIG. 1. Plan view of apparatus. $\check{C}E$ is a Freon-12 threshold Čerenkov counter. $B1$ and $B2$ are small beam-defining counters. V, a 0.5-m^2 counter with a 6-cm^2 hole, vetoes particles from some upstream decays. PR1 and PR2 define a high-momentum proton trajectory. $\check{C}E$ tags electrons from β decays. The 72D18 magnet has $\int \vec{B}\cdot d\vec{l} \simeq 140$ MeV/c; the 48D48 has $\int \vec{B}\cdot d\vec{l} \simeq 450$ MeV/c.

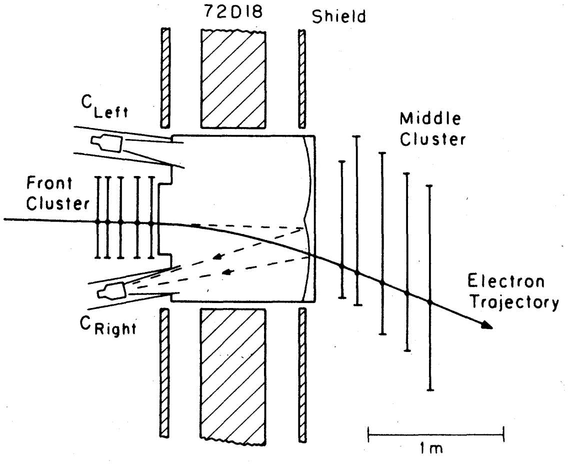

FIG. 2. Plan view of *ČE*, the electron Čerenkov counter, placed between the front and middle clusters of spark chambers. A typical electron trajectory, with typical photons is shown. Photons hitting the right mirror are directed to the right phototube, C_{Right}. Photons hitting the left mirror are directed to the left phototube, C_{Left}.

tion. The tubes have a (118) spectral response extending down to 2200 Å. The mirrors were front-surfaced with aluminum and coated with magnesium fluoride to prevent oxidation. We used cones constructed of aluminized mylar to funnel photons from a 20-cm hole to the 12.6-cm photocathode. The average efficiency of *ČE* on high-β tracks, monitored roughly continuously and carefully daily through the efficiencies for beam π's, was measured to be 0.85 in run B and 0.94 in run C, the data used in our β-decay studies.

The mirrors of *ČE* were aligned with the aid of a Monte Carlo computer program. Since our counter is located in a magnet, it is necessary to include the bending of the electrons in the magnetic field. Electron trajectories from Monte Carlo $\Xi^- \to \Lambda e^- \nu$ events were traced (by computer) through the magnet, and photons were created along the electron paths at appropriate intervals. These photons were then traced through their reflection at the mirrors and to the 20-cm collection holes. In the alignment procedure a laser beam simulated these typical incident photon trajectories at the mirrors, and the mirrors were adjusted to maximize the number of photon trajectories for which light was collected. Typical photons have also been created for electrons from our found β-decay events. These photon distributions from our detected electrons are consistent with the expected distributions. No gross spatial inefficiencies in the Čerenkov-counter electron detection are indicated.

2. *Efficiency and threshold*

We have estimated the efficiency of the counter, using the manufacturer's data for the quantum efficiency of the tube as a function of wavelength. Our calculated result is that a beam pion, which is well above threshold, should yield approximately 7 photoelectrons, whereas we measure an inefficiency of 6%, indicating a yield of only 4 photoelectrons. We attribute this difference to factors such as variation in quantum efficiency. [In light-emitting diode (LED) tests, we have found the quantum efficiency to vary by a factor of 2 over the surface of the photocathode.] From our measured efficiency of 94% for beam pions, predicted collection efficiencies for $\Xi^- \to \Lambda e^- \nu$ and $\Sigma^- \to \Lambda e^- \nu$ are $(95 \pm 4)\%$ and $(92 \pm 5)\%$, respectively.

The above efficiency figures refer to the operation of the counter during run C. The corresponding beam track efficiency for rum B was 85%. The improvement in the efficiency resulted from the re-aluminizing of the mirrors between the two running periods. In our analysis, the ČE efficiency for electrons in the β-decay modes is taken to be the same as that for beam pions, consistent with these results.

The Čerenkov counter was filled with air at atmospheric pressure, and the Čerenkov threshold corresponds to a γ of ≈ 41 (5.7 GeV/c for pions, 0.02 GeV/c for electrons). Electrons which are measurable in our spectrometer (>0.3 GeV/c) are well above this threshold and pions from the normal Ξ and Λ decays are all less than 6 GeV/c. Virtually no muons from decay with $\pi^- \to \mu\nu$ are above 5 GeV/c.

From a sample of about 10 000 reconstructed Σ's, we measured the true Čerenkov threshold. Σ's are an ideal probe for this, because the pions from $\Sigma \to n\pi$ have a momentum range extending both above and below the expected Čerenkov threshold. Since the electronic threshold for the discriminators for this counter was set well below the pulse height corresponding to one photoelectron, we expect the inefficiency to be

$$1 - \epsilon = e^{-\langle N_e \rangle},$$

in which $\langle N_e \rangle = K' \sin^2(\theta)$ is the mean number of photoelectrons produced at the photomultiplier tube, K' is a constant which depends upon our detector, and θ is the Čerenkov angle $\cos(\theta) = c/vn$. Then the inefficiency is

$$1 - \epsilon = e^{-A[B-(m/P)^2]},$$

in which $A = K'/n^2$ and $B = n^2 - 1$, and m and P are the mass and momentum of the particle. Figure 3 is a plot of inefficiency versus $1/P^2$ for pions from $\Sigma^- \to n\pi^-$, together with the beam-pion result. The

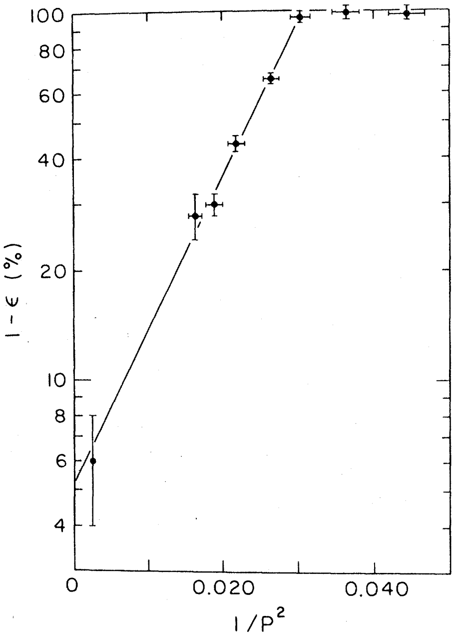

FIG. 3. Electron Čerenkov-counter ($\check{C}E$) inefficiency ($1-\epsilon$) plotted versus $1/p^2$ where p is the momentum of the test particles in GeV. The relationship expected is $1-\epsilon=e^{(a-b/p^2)}$. The straight line is drawn by eye. The physical significance of the constants a and b, read from the graph, is discussed in the text.

inefficiency has been corrected for a 6% background below threshold.

The line in Fig. 3 was drawn by eye. The 100%-inefficiency point gives a pion threshold momentum of 5.74 ± 0.06 GeV/c, corresponding to an index of refraction $n-1=(2.97\pm0.1)\times10^4$. Air at 20°C and wavelength = 2800 Å, typical of the response of our phototubes, has $n-1=2.94\times10^{-4}$, consistent with our measurements.

3. *Timing resolution and backgrounds*

Figure 4 shows time distributions for pulses from the counter $\check{C}E$, relative to the beam coincidence pulse, for various classes of events. The narrow peaks demonstrate an in-time signal, but their width is greater than one expects from the manufacturer's claimed single photoelectron timing width [2.42 ns full width at half maximum (FWHM)]. We attribute this to the variation of the timing properties over the surface of the phototube, and to small changes in the timing during the experiment.

There was a small amount of in-time background due to scintillation and other processes. Studying low-momentum (below Čerenkov threshold) pions from Σ decays provided an excellent test of background rates. Making the requirement that the $\check{C}E$ signal arrive in a 12 nsec interval, and the $\check{C}E$ position information be consistent with the measured position of the pion at the mirror, our total in-time rate was $(5.3\pm0.3)\%$. Looking at late times from timing information gave an accidental rate of $(1.9\pm0.1)\%$. Subtracting, we have $(3.4\pm0.3)\%$ net in-time rate above background (scintillation, etc.) for a single track.

Doing the same for a sample of reconstructed Ξ decays, for which all tracks are below Čerenkov threshold, gave $(6.6\pm0.3)\%$ total in-time rate. The accidental rate was $(2.0\pm0.2)\%$ per 12 nsec. Subtracting gives $(4.6\pm0.4)\%$ net in-time signal above background. (One would expect the scintillation rate for Ξ/Σ to be larger than one, since

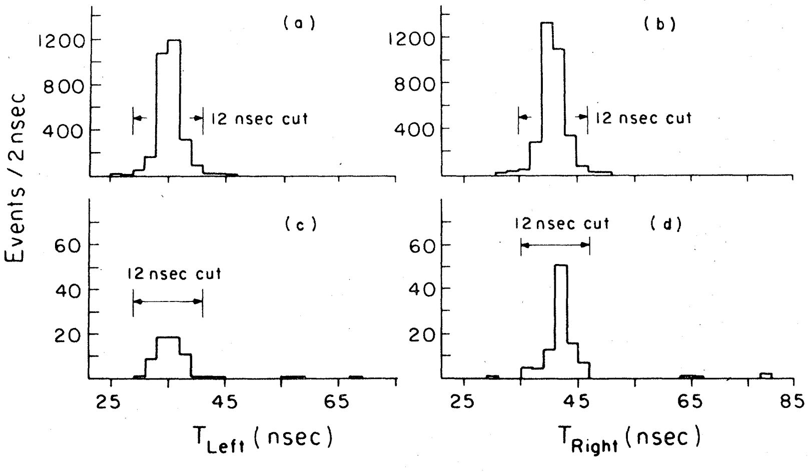

FIG. 4. Timing distributions, with respect to a beam counter, of signals in $\check{C}E$, the electron Čerenkov counter. (a) Beam pions in C_{Left}. (b) Beam pions in C_{Right}. (c) Candidates from final $\Sigma^-\to\Lambda e^-\nu$ sample, C_{Left}. (d) Candidates from final $\Sigma^-\to\Lambda e^-\nu$ sample, C_{Right}.

Λ's from the Ξ decay may decay either upstream or inside of the magnet.) We find a ratio of (1.4 ± 0.5), which seems reasonable.

Using recent measurements on scintillation yields in air of 4.3 photons/meter per particle[29] and making rough estimates of the $\check{C}E$ collection efficiency for isotropically emitted light, we expect the probability for $\check{C}E$ to detect scintillation light to be about 1% per track, comparable to our measured value. Estimates have also been made for $\check{C}E$ triggers from processes such as knock-on electrons; these processes are expected to be negligible compared to the scintillation process.

B. γ detector

The γ detector used in this experiment to search for the decay mode $\Xi^- \rightarrow \Sigma^0 e^- \nu$ was a steel-plate optical spark chamber located downstream of the rear cluster of magnetostrictive spark chambers and centered on the beam line. The chamber consisted of 64 gaps separated by steel plates 1.6 mm (0.086 radiation lengths) thick. It has a cross-sectional area of 1.2 m × 1.2 m, and it was photographed in 90° stereo. The chamber and its characteristics are described in detail in the report of a previous experiment in which it was used with essentially the same optical system.[30] Since the optical system was completely independent of the rest of the experiment, we accepted data for the electronic portion of the experiment even if the optical system developed problems. Also a noise problem existed in the electronics which recorded the contents of the visual data box on magnetic tape resulting in occasional destruction of the correspondence between the electronic data and the photographic records for these reasons. The total efficiency for the optical portion of the experimental data relative to the electronic portion was approximately 63%.

C. Triggers

Our triggering system is described in detail in paper I. Briefly, a hyperon trigger is defined as a track detected in our beam counters but with no count in the beam-channel Čerenkov counter. "Ξ" triggers are defined in our logic as a hyperon in the beam channel plus counters PR1 and PR2 which define a high-momentum trajectory typical of the proton in $\Lambda \rightarrow p\pi^-$ decay. These "Ξ" triggers have a high efficiency for $\Xi \rightarrow \Lambda\pi$ events, form a normalization for β decays, and allow us to study kinematic discrimination against backgrounds. About 25% of our raw data are from "Ξ" triggers.

β-decay triggers ("Ξ" $\cdot \check{C}E$) form the bulk ($\approx$75%) of our data sample. Most of our β-decay candidates come from these triggers. A β-decay trigger is nominally a hyperon (Σ or Ξ) decaying into a Λ, plus another particle triggering the electron Čerenkov counter. Because a number of processes other than β decays may trigger $\check{C}E$, the singles rate in the large volume counter is high, and the $\check{C}E$ requirement reduced "Ξ" triggers by only a factor of 4–5 (trigger rejection). However, as discussed above, timing and position consistency requirements for the $\check{C}E$ signal reduce reconstructed cascades by a factor of 16 (final analysis $\check{C}E$ rejection).

For any hyperon trigger, roughly $\frac{2}{3}$ of the data are from hyperon decays upstream of the fiducial region. For events taken with a "Ξ" trigger which pass the fiducial region test, about $\frac{1}{3}$ are from processes with incident Σ or pion; these often legitimately fire $\check{C}E$, but are effectively removed in the pattern-recognition process. Approximate compositions of "Ξ" and β-decay triggers are given in Table II.

TABLE II. Approximate composition "Ξ" and β decay ("Ξ" $\cdot \check{C}E$) triggers.

Event category \ Trigger	"Ξ"	$\check{C}E$	"Ξ" $\cdot \check{C}E$
Upstream decays	$\frac{2}{3}$	11%	7%
Σ or π processes	$\frac{1}{9}$	94%	11%
Ξ processes	$\frac{2}{9}$	11%	2%
(Consistent with observed $\check{C}E$ $\cdot$ "Ξ"/"Ξ" trigger rates)			20%

III. ANALYSIS METHODS

The pattern recognition of beam $\rightarrow \Lambda +$negative was carried out in the same way for the normal $\Lambda\pi$ decay and the leptonic $\Lambda e^-\nu$ decays. This process is described in detail in paper I. Briefly, the pattern-recognition process involves recognizing a high-momentum positive and combining it with a negative trajectory to find a satisfactory kinematic fit for a Λ. Found Λ's are tested with other negative trajectories. Those Λ-negative pairs which are geometrically consistent with the sequence beam $\rightarrow \Lambda +$negative; $\Lambda \rightarrow p\pi^-$ are retained as "Λ +negative" topologies for analysis of either the $\Lambda\pi^-$ mode or the leptonic modes.

A. Monte Carlo studies

Particle decays of interest ($\Xi^- \rightarrow \Lambda\pi^-$, $\Xi \rightarrow \Lambda e^-\nu$, etc.) were studied by our Monte Carlo process. The decays were simulated, the decay products were traced through the known geometry and boundaries of the apparatus, and fake-data tapes of "measured" sparks generated. These "fake-data tapes" were then analyzed by the same programs as the real data. All decays are generated in the center-of-mass system of the parent particle. For a three-body decay such as $\Sigma^- \to \Lambda e^- \nu$ the momenta of two particles, the Λ and electron, are chosen randomly inside the Dalitz-plot boundary. The three particles lie in a plane in the center of mass of the parent, due to conservation of vector momentum. The orientation of the plane, determined by the three Euler angles, is randomly chosen. Each point on the Dalitz plot is assigned a weight, either constant over the Dalitz plot or based upon the value of $|M|^2$, the square of the matrix element at that point, evaluated with specific values of the form factors. The momentum transformations and tracing through the apparatus are performed as in the two-body decay.

Comparsions of the fake-data distributions with real data give confidence in the analysis programs and firmer understanding of the effects of the selection criteria and measurement errors. The fake-data analysis is used in the study of the form factors in the $\Sigma^- \to \Lambda e^- \nu$ decay, as well as in determining the efficiencies used in the branching-ratio calculations for the Ξ and the Σ leptonic decays.

B. $\Xi \to \Lambda\pi$

Since the pattern recognition is similar, we have studied the two-body $\Xi^- \to \Lambda\pi^-$ in some detail to gain confidence in the Monte Carlo simulation of our detection efficiency, resolution, and biases. This study was reported in large part in paper I. However, in this section we discuss in detail some tests of particular interest in the separation of the β-decay modes from the large number of background decays. For our comparison of $\Lambda\pi$ results with the fake-data Monte Carlo, we select $\Lambda\pi^-$ topology events from "Ξ" triggers (no $\check{C}E$ required). There were 4462 of these from run B "Ξ" triggers, and 3718 from run C triggers for a total of 8180. For each histogram we show, the smooth curve is obtained from our Monte Carlo fake data.

Figure 5 shows the "momentum imbalance," the difference between the beam particle and $\Lambda + \pi$ momentum. We define the imbalance as

$$\Delta\vec{P}_{\text{beam}} - (\vec{P}_\Lambda + \vec{P}_p) .$$

For a β-decay event $\Delta\vec{P}$ is the neutrino momentum. For a normal decay $\Delta\vec{P}$ should be zero. The spread in the components of $\Delta\vec{P}$ is caused by measurement errors. The vertical component [ΔP_y, shown in Fig. 5(b)] with almost no magnetic bending is well fitted by the fake-data curve. The horizontal component [ΔP_z, shown in Fig. 5(c)] in the plane of the magnetic bending is somewhat narrower for the real data than for the fake-data distribution, while the component along the beam line [ΔP_x, shown in 5(a)] is somewhat narrower for the fake-data analysis than for the Monte Carlo events. Figure 6 is the square of the "missing four-momentum":

$$M_X^2 = (E_{\text{beam}} - E_\Lambda - E_{\text{neg}})^2 - |\Delta\vec{P}|^2 .$$

For normal $\Xi^- \to \Lambda\pi^-$ decays, properly interpreted, M_X^2 is zero (to within measuring errors). Our real data agree with the Monte Carlo data, indicating a resolution for M_X^2 of approximately 0.004 GeV^2.

Figure 7 shows the distribution of the kinetic energies of the Λ and the pion in the center-of-

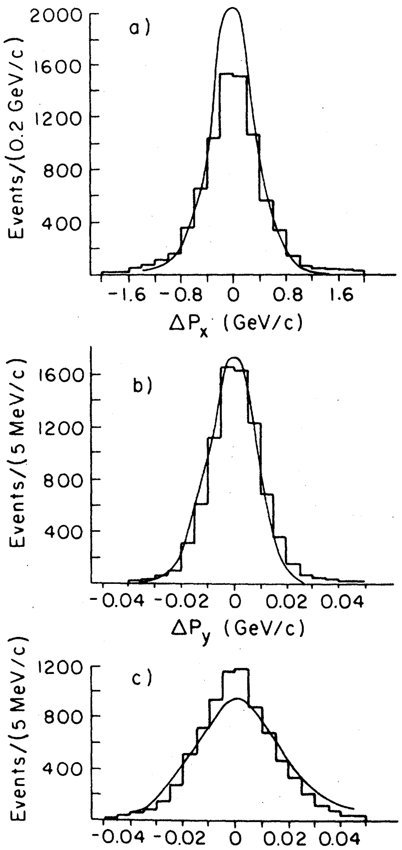

FIG. 5. $\Delta\vec{P}$, the momentum inbalance between the beam particle and the final state $\Lambda\pi^-$, for 8180 normal $\Xi^- \to \Lambda\pi^-$ decays. (a) ΔP_x, the component along the beam. (b) ΔP_y, the transverse component in the vertical (nonbending) plane of the spectrometer magnets. (c) ΔP_z, the transverse component in the horizontal (bending) plane of the spectrometer magnets.

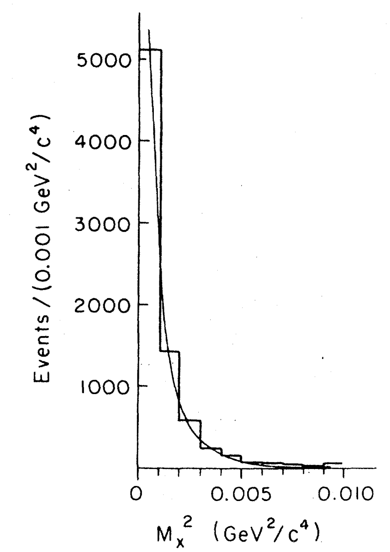

FIG. 6. $M_X{}^2$, the missing mass squared: $(\Xi - \Lambda - \pi)^2$, for 8180 normal $\Xi^- \rightarrow \Lambda\pi^-$ decays.

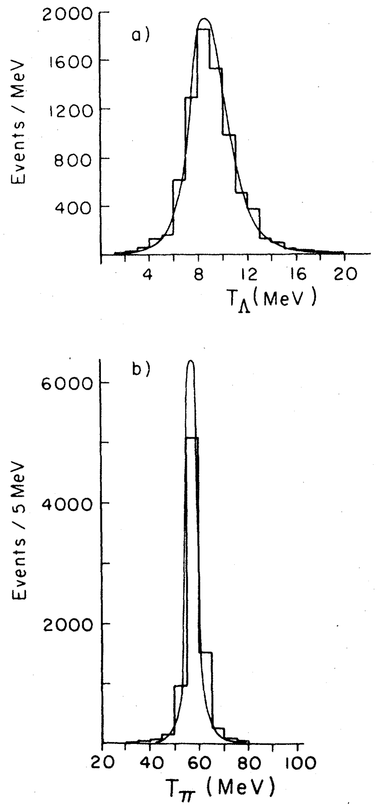

FIG. 7. Kinetic energy of the Λ and the pion in the Ξ^- center of mass, for 8180 $\Xi^- \rightarrow \Lambda\pi^-$ normal decays. (a) Kinetic energy of the Λ. (b) Kinetic energy of the pion.

mass system for $\Xi \rightarrow \Lambda\pi$. We expect the kinetic energies to peak at $T_\Lambda = 8.6$ MeV, and $T_\pi = 57.3$ MeV. Again the fake (or Monte Carlo) data are consistent with our results.

The next two figures emphasize the kinematic overlap between the $\Xi \rightarrow \Lambda\pi$ decays and $\Xi^- \rightarrow \Lambda e^-\nu$, $\Sigma^- \rightarrow \Lambda e^-\nu$. Without the 20-MeV $\Lambda\pi$ mass cut to remove normal Ξ decays, we would be unable to separate the decays kinematically at the required level. Figure 8(a) shows the Daltz plot of $\Xi^- \rightarrow \Lambda\pi^-$ interpreted as $\Sigma^- \rightarrow \Lambda e^-\nu$ and Fig. 8(b) shows the Dalitz plot of $\Xi^- \rightarrow \Lambda\pi^-$ interpreted as $\Xi^- \rightarrow \Lambda e^-\nu$ (i.e., we assign the electron mass to the negative track). For the $\Xi^- \rightarrow \Lambda e^-\nu$ the events peak in one part of the Dalitz plot. Our 20-MeV mass cut should eliminate much of this $\Xi^- \rightarrow \Lambda\pi^-$ background, but it will also deplete that part of the Dalitz plot which is populated by these misinterpreted events. For the $\Sigma^- \rightarrow \Lambda e^-\nu$ interpretation, we see that about 8% of the $\Lambda\pi^-$ events are kinematically ambiguous with $\Sigma^- \rightarrow \Lambda e^-\nu$ (i.e., lie within the $\Sigma^- \rightarrow \Lambda e^-\nu$ Dalitz plot).

C. β-decay separation

To obtain a relatively clean sample of $\Sigma^- \rightarrow \Lambda e^-\nu$ and $\Xi^- \rightarrow \Lambda e^-\nu$, we impose a series of kinematic and $\check{C}E$ consistency cuts. The cuts used are the following.

(1) With the event treated as a $\Lambda\pi^-$ final state,

$$|M_{\Lambda\pi^-} - 1.321| > 0.02 \text{ GeV}/c^2 .$$

The observed 1/30 of $\Xi^- \rightarrow \Lambda\pi^-$ topologies beyond the $\Lambda\pi^-$ mass cut include beta decays we seek, misreconstructed $\Xi^- \rightarrow \Lambda\pi^-$ events, and other potential background events. Figure 9(a) shows $M_{\Lambda e\nu}$ for all bad events, and Fig. 9(b) displays $M_{\Lambda e\nu}$ for all badly fitting $\Xi^- \rightarrow \Lambda\pi^-$ topology events (i.e., $|M_{\Lambda\pi^-} - 1.321| > 0.02$ GeV/c^2).

(2) $\check{C}E$ spatial and timing information must be consistent with the electron trajectory. 96% of the β-decay candidates survive these cuts, and this reduces our $\Xi^- \rightarrow \Lambda\pi^-$ background from 11% to 6% of the kinematic overlap.

(3) We assign a hyperon mass (Ξ or Σ) to the beam particle and an electron mass to the negative track, and calculate

$$M_\nu{}^2 = (E_{\text{beam}} - E_\Lambda - E_e)^2 - |\Delta \vec{P}|^2 .$$

We demand that $M_\nu{}^2$ (for one of the two incident-particle hypotheses) satisfy

$$|M_\nu{}^2| < 0.004 \text{ GeV}^2 .$$

This criterion selects possible candidates for the β-decay modes.

(4) We now assume $M_\nu = 0$ and calculate

$$M_{\Lambda e\nu}{}^2 = (E_\Lambda + E_e + |\Delta\vec{P}|)^2 - P_{\text{beam}}{}^2 ,$$

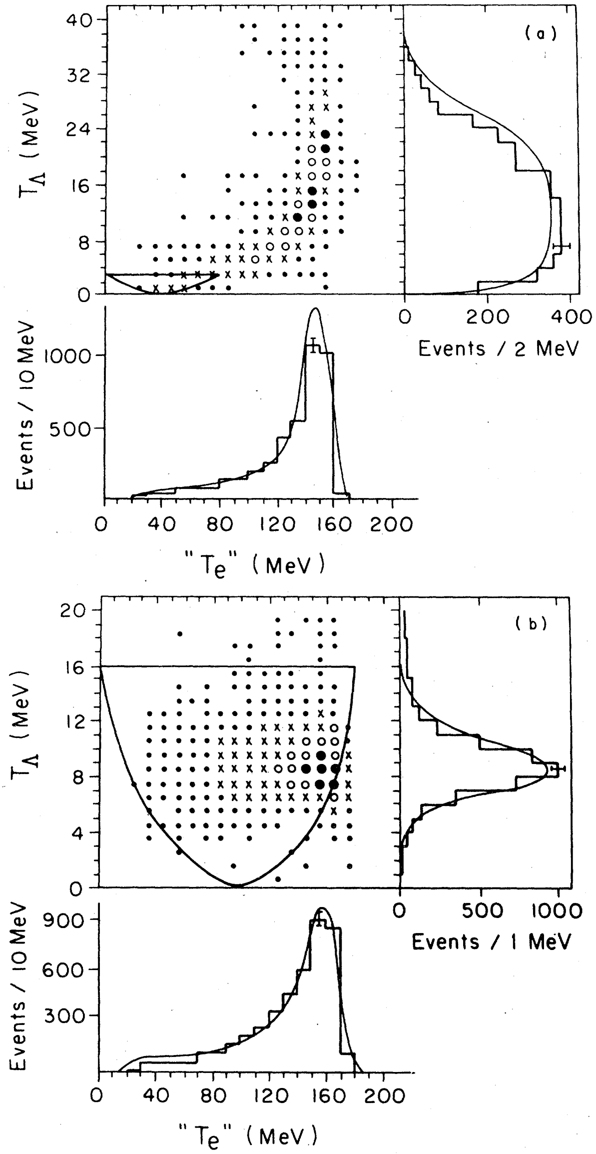

FIG. 8. Monte Carlo results of generated $\Xi^- \to \Lambda\pi^-$ decays, treated as (a) $\Sigma^- \to \Lambda e^- \nu$ or (b) $\Xi^- \to \Lambda e^- \nu$. T_Λ and "T_e", the kinetic energy for that pion interpreted as an electron, are included, as well as their correlations. The Dalitz-plot boundaries are shown on the scatter plot for T_Λ and "T_e". The key to the symbols in (a) is: •: < 30 events; ×: 30 < No. of events < 100; ○: 100 < No. of events < 150; and ●: > 150 events. The key to the symbols in (b) is: •: < 30 events; ×: 30 < No. of events < 100; ○: 100 < No. of events < 200; and ●: > 200 events.

from the measured kinematic quantities. For $\Sigma \to \Lambda e\nu$ candidates we require

$$1.167 < M_{\Lambda e\nu} < 1.227 \text{ GeV}/c^2$$

and for $\Xi \to \Lambda e\nu$ we require

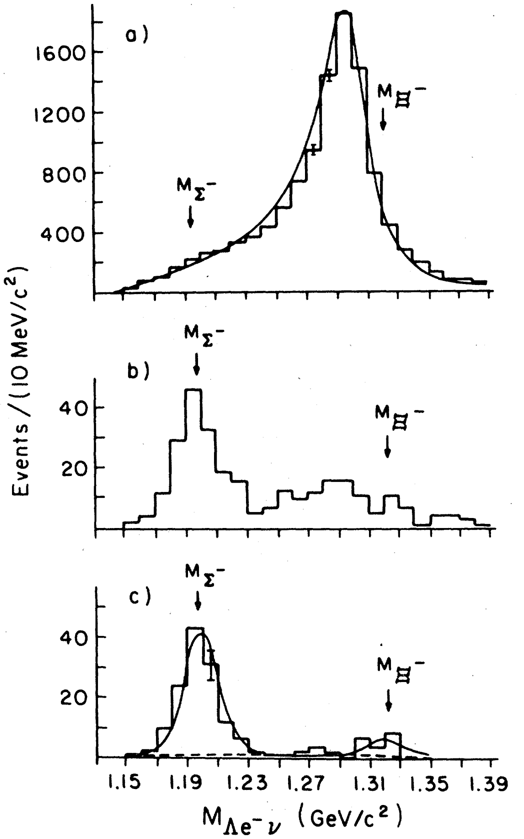

FIG. 9. $M_{\Lambda e^- \nu} = [(E_\Lambda + E_e + E_\nu)^2 - (\vec{P}_{\text{beam}})^2]^{1/2}$ where $E_\nu = |\vec{P}_{\text{beam}} - \vec{P}_\Lambda - \vec{P}_e|$, E_e is the energy of the electron candidate interpreted as an electron, E_Λ is the energy of the Λ, and $\vec{P}_{\text{beam}}$, $\vec{P}_\Lambda$, and $\vec{P}_e$ are the momenta of the beam particle, Λ and "electron", respectively. Note that $M_{\Lambda e^- \nu}$ is independent of the mass of the beam particle. (a) 25 000 normal $\Xi^- \to \Lambda\pi^-$ decays from both "Ξ" and "Ξ"$\cdot \check{C}E$ triggers, the entire runs B and C reconstructed $\Lambda\pi^-$ sample. (b) $M_{\Lambda e^- \nu}$ for the events in (a) which satisfy P_e and opening angle cuts as well as $|M_{\Lambda\pi} - {=}1.321 \text{ GeV}/c^2| > 0.20 \text{ GeV}/c^2$, where $M_{\Lambda\pi}$ is the effective mass of the $\Lambda\pi$. (c) $M_{\Lambda e^- \nu}$ for the events in (b) which satisfy the final $\check{C}E$ and $M_\nu{}^2 = (E_{\text{beam}} - E_\Lambda - E_e)^2 - (\vec{P}_{\text{beam}} - \vec{P}_\Lambda - \vec{P}_e)^2$ cuts and survive hand examination for consistent topology. The solid curve is the prediction for background plus $\Sigma^- \to \Lambda e^- \nu$, $\Xi^- \to \Lambda e^- \nu$ events. The dashed curve represents expected background (from $\Xi^- \to \Lambda\pi^-$ in the $\Sigma^- \to \Lambda e^- \nu$ region and from $\Xi^- \to \Lambda\pi$, $\Sigma^- \to \Lambda e^- \nu$, and $\Xi^- \to \Sigma^0 e\nu$ in the $\Xi^- \to \Lambda e^- \nu$ region).

$$1.311 < M_{\Lambda e\nu} < 1.351 \text{ GeV}/c^2 .$$

The Ξ $M_{\Lambda e\nu}$ cuts are chosen asymmetrically to avoid backgrounds below the Ξ mass. The momentum of the electron is also required to be above 0.4 GeV/c^2. Very few trajectories with topology <0.3 GeV/c^2 will pass through the magnet to the middle cluster of spark chambers, and

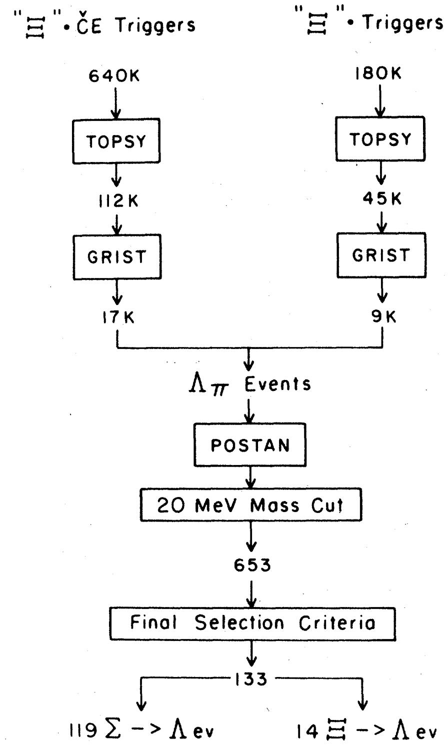

FIG. 10. Data flow in the experiment.

some inefficiency is suspected for trajectories with momentum between 0.3 and 0.4 GeV/c. After removal of two recognized bad topology $\Sigma^- \to \Lambda e^-\nu$ events and two $\Xi^- \to \Lambda e^-\nu$ events, these cuts leave 119 $\Sigma^- \to \Lambda e^-\nu$ and 14 $\Xi^- \to \Lambda e^-\nu$. After removal of recognized bad topology events, the final sample is shown in Fig. 9(c). Figure 10 shows the data flow.

We have measured background to the β-decay modes by looking at 8100 reconstructed $\Xi^- \to \Lambda\pi^-$ from 200 000 "Ξ" triggers ($\check{C}E$ not required). Twenty events pass the kinetic criteria for $\Sigma^- \to \Lambda e^-\nu$ of which ten have no $\check{C}E$ count. The ten with a $\check{C}E$ count are statistically consistent with the number expected for this decay; the expected number of good events missed due to measured $\check{C}E$ inefficiency on high-β tracks is expected to be approximately equal to the number of real $\Lambda\pi^-$ events accepted by our selection criteria but with false $\check{C}E$ counts. Only those events with no $\check{C}E$ count are included as kinematic background. For $\Xi^- \to \Lambda e^-\nu$ only 1 event simulates a β decay. This event does not have a $\check{C}E$ count and is taken as indicative of the kinematic background. Combining the observed kinematic rejection with the ČE rejection of $\frac{1}{18}$ and the β-decay detection efficiency, we estimate an experimental upper limit on all forms of false $\check{C}E$ background of about (1 ± 1) of the observed $\Xi^- \to \Lambda e^-\nu$ sample and about (9 ± 3) of the final $\Sigma^- \to \Lambda e^-\nu$ sample.

We have also made Monte Carlo studies of various background processes. Because of our kinematic cuts and the small rates of the processes themselves, $\Lambda \to p e^-\nu$ and $\Xi^- \to \Lambda\mu^-\nu$ give negligible backgrounds. A major source of background is $\Xi^- \to \Lambda\pi^-$ accompanied by a false $\check{C}E$ count. This background may arise from mismeasurement or multiple scattering of the tracks or from $\pi \to \mu\nu$ decay since a track assigned a wrong momentum may cause the event to simulate a β decay. The background from the normal $\Xi^- \to \Lambda\pi^-$ decay is estimated from our fake-data $\Xi^- \to \Lambda\pi^-$ analysis. For the $\Xi^- \to \Lambda e^-\nu$ case we would expect 2.6 events which are recognizable as wrong topologies and 0.9 which could not be recognized as background. This is consistent with our finding of 2 events with recognizable wrong topologies in our $\Xi^- \to \Lambda e^-\nu$ final sample. For the $\Sigma^- \to \Lambda e^-\nu$ case we expect about 1 event which is recognizable as a wrong topology and five events which could not be recognized as background. This is consistent with our finding of 2 events with recognizable wrong topology in our final $\Sigma^- \to \Lambda e^-\nu$ sample. In the following analysis we remove events recognized as wrong topology events and consider background to be from only unrecognizable background events.

There is also small background in the $\Xi^- \to \Lambda e^-\nu$ sample from Σ^- β decays ($\approx$1.3% of the Σ β-decay events within our $\Sigma^- \to \Lambda e^-\nu$ cuts, or $\approx$1.5 events in the $\Xi^- \to \Lambda e^-\nu$ sample). From the Cabibbo prediction for $\Xi^- \to \Sigma^0 e^-\nu$ we would expect about $1\,\Xi \to \Sigma^0 e^-\nu$ event to pass our analysis cuts. Table III gives a summary of background processes and their contribution to our leptonic samples. From the numbers in Table III, we expect a total unrecognized background of 3.4 ± 1.7 events in $\Xi^- \to \Lambda e^-\nu$ and 5 ± 1.5 events in $\Sigma^- \to \Lambda e^-\nu$. Thus, after background subtraction, our final estimate of true β-decay events in our cuts is

$$114\pm 11\ \Sigma^- \to \Lambda e^-\nu\,,$$

$$10.6\pm 3.8\ \Xi^- \to \Lambda e^-\nu\,.$$

These Monte Carlo background estimates are consistent with the experimental estimate described above. The Monte Carlo $M_{\Lambda e\nu}$ distribution for leptonic events plus background agrees well with the $M_{\Lambda e\nu}$ distribution of our observed events. The dashed curves in Fig. 9(c) show the result of the Monte Carlo calculation for the background and the solid curve is the expected $M_{\Lambda e\nu}$ distribution for the signal plus background.

TABLE III. Approximate composition of reconstructed $\Xi^- \to \Lambda\pi$ topology events[a] from Ξ triggers, with $\check{C}E$ and kinematic background estimates. The approximate fraction of events in the final $\Xi^- \to \Lambda e\nu$ candidate sample can be found by multiplying contents of columns (A), (B), and (C); approximate fraction of events in the final $\Sigma^- \to \Lambda e\nu$ sample can be found by multiplying contents of columns of (A), (B), and (D).

Process	(A) No cuts	(B) Fraction of (A) in $\check{C}E$ cuts	(C) Fraction of (A) in kinematic cuts ($\Xi^- \to \Lambda e\nu$)	(D) Fraction of (A) in kinematic cuts ($\Sigma^- \to \Lambda e\nu$)
Rough breakdown[b]				
$\Xi^- \to \Lambda\pi$	97%[c]	0.062[c]	0	0
All backgrounds	3%[c]	0.062	0.007 ± 0.005[c]	0.029 ± 0.011[c]
Misreconstructed $\Xi^- \to \Lambda\pi$[b]				
$\Xi^- \to \Lambda\pi$ (Pattern errors)	~1%[c]	0.062	0.02[c,e]	0.04[c,e]
$\Xi^- \to \Lambda\pi_{\searrow \mu\nu}$	2–3%[d]	0.062	~0.01[d]	~0.025[d]
Other processes[b]				
$\Sigma^- \to \Lambda e\nu$	~0.25%	0.9	0.003[d]	0.31[d]
$\Xi^- \to \Lambda e\nu$	~0.03%	0.9	0.29[d]	$\lesssim$0.002[d]
$\Xi^- \to \Lambda\mu\nu$	$\lesssim$0.04%	0.062	0.06[d]	0.04[d]
$\Xi^- \to \Lambda\pi^- \searrow \left\{\begin{matrix} pe^-\nu \\ p\pi^-\gamma \end{matrix}\right.$	~0.07%	0.9	<0.003[d]	<0.003[d]
$\Xi^- \to \Sigma^0 e\nu$	$\lesssim$0.008%[f]	0.9	0.10[d]	0.03[d]

[a] Our data sample corresponds to 1.23×10^5 effective reconstructed $\Xi^- \to \Lambda\pi$, without $\check{C}E$ cuts.

[b] In the "Rough breakdown" category, events are classified as "$\Xi^- \to \Lambda\pi$" or "all backgrounds" according to whether they pass or fail the criterion $|m_{\Lambda\pi} - 1.321| < 0.020$ GeV/c^2. For the processes in categories "misreconstructed $\Xi^- \to \Lambda\pi^-$" and "other processes", no $m_{\Lambda\pi}$ cut is included in column (A), but the $m_{\Lambda\pi}$ cut is included with other kinematic cuts in column (C).

[c] Experimentally measured numbers.

[d] Results from Monte Carlo program calculations.

[e] Before hand inspection and removal of bad topologies; recognized bad topologies have been removed from other entries in this column.

[f] Cabibbo predictions (Refs. 10 and 11).

IV. RESULTS

A. $\Sigma^- \to \Lambda e^-\nu$ and $\Xi^- \to \Lambda e^-\nu$ branching ratios

The Dalitz plot for the 119 events in our final $\Sigma^- \to \Lambda e^-\nu$ sample is shown in Fig. 11 along with the Monte Carlo distribution normalized to 119 events. Figure 11(b) gives the efficiency for $\Sigma^- \to \Lambda e^-\nu$ detection over the Dalitz plot. In the Monte Carlo calculation used for comparison with these events, we have used both a uniform Dalitz plot and $g_V/g_A = 0$. Except for T_Λ (and in Fig. 19, Λ helicity) where both curves are given, the curves are insensitive to the assumed form of the matrix element. The Monte Carlo curves are for events passing the same requirements as for our data (good geometry, $\Lambda\pi$ mass 20 MeV beyond 1.321 GeV, $|\vec{P}_e| > 0.4$ GeV/c, and $|M_\nu|^2 < 0.004$ GeV^2). Most of the events are within the boundary, and the spreading in T_Λ is explained by our resolution. Figure 12(a) shows the laboratory momenta of the observed Λ's and Fig. 12(b) shows the laboratory momenta of the electrons in our final $\Sigma^- \to \Lambda e^-\nu$ sample. The experimental data are in reasonable agreement with the expected distributions.

The normal $\Xi^- \to \Lambda\pi^-$ decay is expected to be coplanar because of momentum conservation. For a β decay, the three "visible" particles, the beam particle, the Λ, and the electron, are not necessarily coplanar. The coplanarity angle is defined as the angle between the two vectors:

$$\vec{P}_{\text{beam}} \times \vec{P}_{\text{neg}} \text{ and } \vec{P}_{\text{beam}} \times \vec{P}_\Lambda .$$

A coplanar event has a coplanarity angle of 180°.

Figure 13(a) shows the coplanarity angle for the normal decay and Fig. 13(b) shows the coplanarity

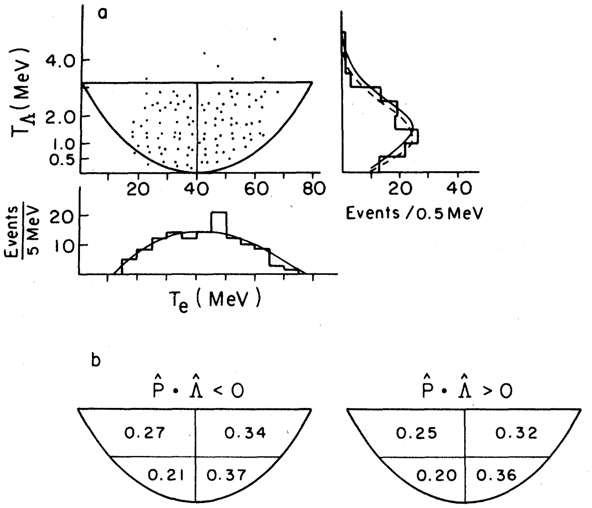

FIG. 11. (a) T_Λ and T_e distributions in the Σ center of mass, for $\Sigma^- \to \Lambda e^- \nu$ candidates. Correlations over the Dalitz plot are also shown. The solid lines drawn in for T_Λ and T_e represent the fake-data prediction for events generated with a uniform Dalitz plot. The dashed line for T_Λ is the fake-data prediction for events generated with the Cabibbo prediction of $g_V = 0$. On this scale, the Cabibbo prediction for T_e is indistinguishable from the uniform-Dalitz-plot T_e prediction. (b) $\Sigma^- \to \Lambda e^- \nu$ detection efficiency over the Dalitz plot, for positive and negative Λ helicity.

angle for $\Sigma^- \to \Lambda e^- \nu$. Both the normal-decay coplanarity distribution (sharply peaked at zero) and the broader β-decay coplanarity distributions are well reproduced by the Monte Carlo.

The distributions of the three components of $\Delta\vec{P}$ the measured neutrino momentum for $\Sigma^- \to \Lambda e^- \nu$, $\Xi^- \to \Lambda e^- \nu$) for these events are shown in Fig. 14.

Since there are only 14 events in our final sample of $\Xi^- \to \Lambda e^- \nu$ candidate, there is little statistical value in comparing details of the distributions with the corresponding Monte Carlo calculations. In this case we have used $g_A/g_V = 0.2$ (the Cabibbo prediction) in the Monte Carlo. Figure 15(a) shows the 14 events (with an estimated background of 3.4 events) on a Dalitz plot. The distributions expected for the background events and for background plus real data are shown in the curves for T_Λ and T_e. Figure 15(b) indicates the efficiency of event detection over the Dalitz plot.

To get the branching ratio $\Xi^- \to \Lambda e^- \nu / \Xi^- \to \Lambda \pi^-$ we take the ratio of observed β decays to the total number of equivalent normal decays, corrected for detection efficiencies:

$$\frac{\Xi^- \to \Lambda e^- \nu}{\Xi^- \to \Lambda \pi^-} = \frac{(\Xi^- \to \Lambda e^- \nu)_{\text{obs}}(1/\epsilon_B)(1/\epsilon_C)(1/B)}{(\Xi \to \Lambda \pi)_{\text{equiv obs}}(1/\epsilon_n)(1/B)}$$

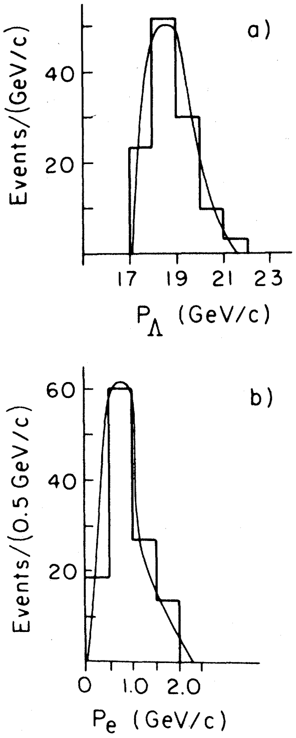

FIG. 12. (a) Λ momenta for the 119 final $\Sigma^- \to \Lambda e^- \nu$ events. (b) Electron momenta for the 119 final $\Sigma^- \to \Lambda e^- \nu$ events; the cuts are discussed in detail in the text. The 0.4 GeV/c lower limit on $\vec{P}_e$ has been made; thus the effective lower limit on the lowest P_e bin is 0.4 GeV/c. For both (a) and (b) the solid curve is the prediction for uniform Dalitz-plot efficiency. On this scale the Cabibbo prediction is undistinguishable from the curve drawn.

in which

$(\Xi^- \to \Lambda e^- \nu)_{\text{obs}} = (14 \pm 4) - (3.4 \pm 1.5)$ (subtraction for $\Xi^- \to \Lambda \pi^-$, $\Sigma^- \to \Lambda e^- \nu$, $\Xi^- \to \Sigma^0 e^- \nu$ background),

$\epsilon_\beta = \epsilon_{\beta 1}\epsilon_{\beta 2} = 0.08$; $\epsilon_\beta/\epsilon_n = 0.29 \pm 0.03$,

$\epsilon_{\beta 1}$ = geometric detection efficiency for ($\Xi^- \to \Lambda e^- \nu$) ~ 0.52,

$\epsilon_{\beta 2}$ = analysis detection efficiency for ($\Xi^- \to \Lambda e^- \nu$) ~ 0.15,

$\epsilon_C = \check{C}E$ efficiency = 0.85 for run B, 0.94 for run C,

$B = (\Lambda \to p\pi)/(\Lambda \to \text{all}) = 0.64$,

$\epsilon_n = \epsilon_{n1}\epsilon_{n2} = 0.275$,

ϵ_{n1} = geometrical efficiency for ($\Xi \to \Lambda\pi$) ~ 0.67,

ϵ_{n2} = analysis efficiency for ($\Xi \to \Lambda\pi$) ~ 0.41.

The detection efficiencies ϵ_{n1}, ϵ_{n2}, $\epsilon_{\beta 2}$ were obtained from Monte Carlo studies. The efficiency ϵ_β is not very sensitive to the exact value of the form factors g_V, g_A, and g_{WM}; changing the form factors from pure Cabibbo prediction to uniform Dalitz plot results in a change in ϵ_β by less than ≈10%. Our calculation is an average of a uniform-

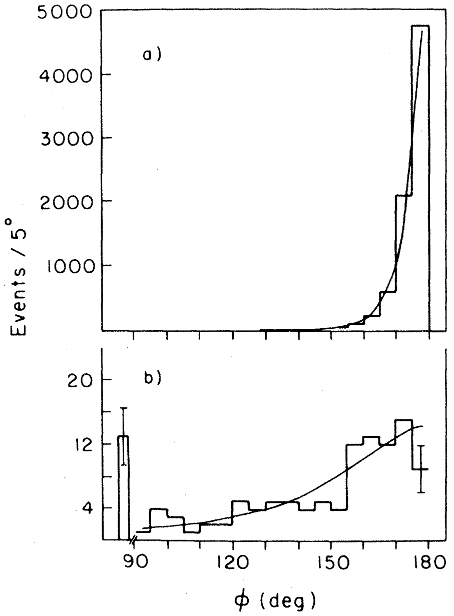

FIG. 13. ϕ, the coplanarity angle: $(\vec{P}_{beam}\times\vec{P}_\Lambda)\cdot(\vec{P}_{beam}\times\vec{P}_{neg})/|\vec{P}_{beam}\times\vec{P}_\Lambda||\vec{P}_{beam}\times\vec{P}_{neg}|=\cos\phi$. (a) The 8180 normal $\Xi^-\to\Lambda\pi^-$ events. The solid curve is the Monte Carlo prediction. (b) The final sample of 119 $\Sigma^-\to\Lambda e^-\nu$ candidates. The solid curve is the prediction for uniform Dalitz-plot efficiency. On this scale the Cabibbo prediction is indistinguishable from the curve drawn.

Dalitz-plot and a Cabibbo-prediction result:

$(\Xi^-\to\Lambda\pi^-)_{\text{equiv obs}}=$No. of equivalent "$\Xi$" triggers $\times\,\epsilon_R$ where $\epsilon_R=0.046\pm0.003$ is the fraction of "Ξ" trigger events reconstructed in analysis as $\Xi^-\to\Lambda\pi$,

No. of equivalent "Ξ" triggers $=$No. of "Ξ" triggers $+[R\times$ (No. of "Ξ" $\cdot\,\check{C}E$ triggers)], where $R=$ratio of "Ξ" to "Ξ" $\cdot\,\check{C}E$ triggers, monitored continuously,

$\epsilon_C=0.85$ for run B data, 0.94 for run C data, $R\approx4.5$,

No. of "Ξ" triggers $=5.6\times10^4$ (run B) $+8.2\times10^4$ (run C),

(No. of "Ξ" $\cdot\,\check{C}E$ triggers) $\times R=1.1815\times10^6$ (run B) $+1.542\times10^6$ (run C). The number of equivalent Ξ triggers $\times\,\epsilon_C$ is thus

$$[(1.237\times10^6)\times(0.85)]+[(1.724\times10^6)\times(0.94)]=2.67\times10^6\,.$$

Then, equivalent reconstructed $\Xi^-\to\Lambda\pi^-$ events, including Čerenkov-counter efficiency, $=2.67\times10^6\times0.046=(1.23\pm0.08)\times10^5$. Our result for the branching ratio then becomes

$$\frac{\Xi^-\to\Lambda e^-\nu}{\Xi^-\to\Lambda\pi^-}=\frac{(10.6\pm4.2)}{(0.29\pm0.03)\times(1.23\pm0.08)\times10^5}=(0.30\pm0.13)\times10^{-3}\,.$$

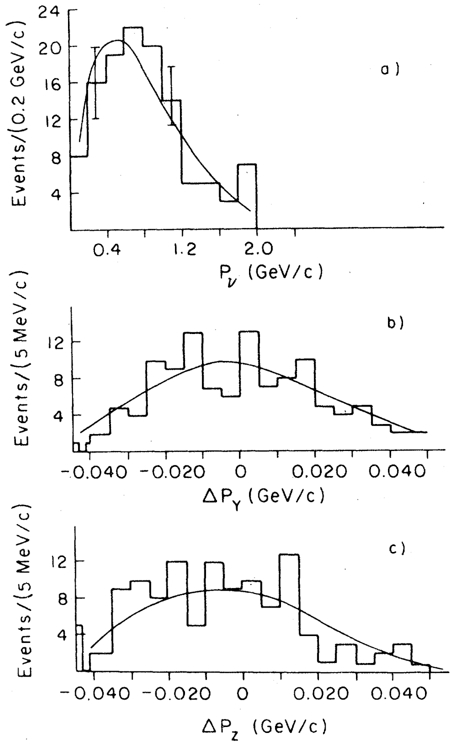

FIG. 14. $\vec{P}_\nu=\Delta\vec{P}=\vec{P}_{beam}-\vec{P}_\Lambda-\vec{P}_e$ for the final 119 $\Sigma^-\to\Lambda e^-\nu$ candidate sample. (a) The component along the beam line; this is nearly the total neutrino momentum and is labeled P_ν. (b) The component in the vertical (transverse, nonbending) plane of the spectrometer. (c) The component in the horizontal (transverse, nonbending) plane of the spectrometer. The solid curves are the Monte Carlo curves from the fake data and are insensitive to the form factors. The Monte Carlo curve for (a) is quite sensitive to the assumed apparatus resolution and the central beam momentum. The Monte Carlo was tuned on the normal $\Xi^-\to\Lambda\pi^-$ decay.

The error is dominated by the statistical error in the observed 14 candidates.

The $(\Sigma^-\to\Lambda e^-\nu)/(\Sigma^-\to n\pi^-)$ branching ratio is calculated in a similar fashion. As with $\Xi^-\to\Lambda e^-\nu$, ϵ_β is not very sensitive to the form factors. We assumed an average of the uniform Dalitz result and the Cabibbo prediction in our result. In addition, since we normalized to $\Xi^-\to\Lambda\pi^-$ decays, we must include the Σ/Ξ ratio to get the equivalent number of Σ's.

For Σ^-/Ξ ratios, we use 47 ± 5 for the downstream Al_2O_3 data and 59 ± 8 for the upstream Al data. A weighted average yields 47.4, since 98.5% of the data was taken downstream Al_2O_3 target. We have

$\Sigma^-\to\Lambda e^-\nu=(\Sigma\to\Lambda e^-\nu)_{\text{obs}}(1/\epsilon_\beta)(1/\epsilon_C)(1/B)$,

$\Sigma^-\to n\pi^-=$(No. of equivalent "Ξ" triggers) $\times\,(\Sigma/\Xi)(\epsilon_R)(1/\epsilon_n)(1/B)$,

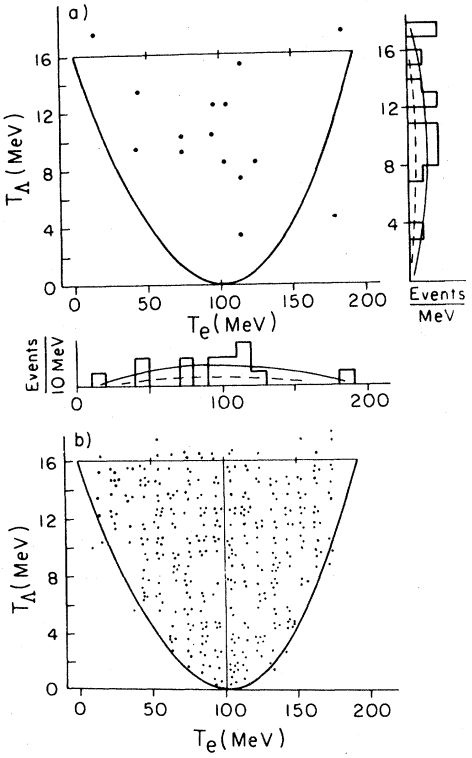

FIG. 15. (a) Dalitz plot for our final sample of 14 $\Xi^- \rightarrow \Lambda e^- \nu$ candidates. The dashed lines for T_Λ, T_e indicate background from $\Xi^- \rightarrow \Lambda \pi^-$, $\Sigma^- \rightarrow \Lambda^0 e^- \nu$, and $\Xi^- \rightarrow \Sigma^0 e^- \nu$. The solid lines include the combination of background and the signal expected, with our observed ratio but the Cabibbo prediction of $g_V/g_A = 0.2$ for the Dalitz-plot prediction. (b) Reconstructed distribution of Monte Carlo $\Xi^- \rightarrow \Lambda e^- \nu$ events. The events were generated uniformly over the Dalitz plot, and their rather uniform final reconstructed distribution is an indication of the relative uniformity and lack of bias in detection over the Dalitz plot.

$$N_{\text{obs}} = (119 \pm 11) - (4.9 \pm 1.7) \text{ (background)},$$
$$\epsilon_\beta/\epsilon_n = 0.31 \pm 0.02,$$

$$\frac{\Sigma \rightarrow \Lambda e^- \nu}{\Sigma \rightarrow n\pi} = \frac{(114 \pm 11.3)}{(1.23 \pm 0.08) \times 10^5 (47.5 \pm 0.5)(0.31 \pm 0.02)}$$
$$= (0.63 \pm 0.11) \times 10^{-4}.$$

These are our final values for the $\Xi^- \rightarrow \Lambda e^- \nu$ and $\Sigma^- \rightarrow \Lambda e^- \nu$ branching ratios; they are consistent with but supersede those in our preliminary report.[31] The largest changes in the present analysis are (1) removal of events with $P_e < 0.4$ GeV/c and (2) a more careful study of detection efficiency, including complete analysis reconstruction of Monte Carlo events. Our preliminary quoted errors were statistical, with rough estimates of systematic errors discussed in the text. The errors quoted in this report include both statistical and systematic errors (12% for $\Xi^- \rightarrow \Lambda e^- \nu$ and 14% for $\Sigma^- \rightarrow \Lambda e^- \nu$) added in quadrature. The detection efficiency is not very dependent on the form factors. Since we normalize our two β-decay modes to $\Xi^- \rightarrow \Lambda\pi$, the absolute $\Lambda\pi$ detection efficiency is not necessary, but only the relative efficiency of the β-decay modes to the normal $\Xi^- \rightarrow \Lambda\pi$ mode. These relative efficiencies are rather insensitive ($\lesssim 10\%$) to form factors in the β decays or to small changes in assumptions about spark-chamber measurement resolution. The $\Sigma^- \rightarrow \Lambda e^- \nu$ normalization error is larger than that for $\Xi^- \rightarrow \Lambda e^- \nu$ because of inclusion of uncertainty in the Σ/Ξ ratio. For $\Sigma^- \rightarrow \Lambda e^- \nu$, normalization and statistical errors are comparable. For $\Xi^- \rightarrow \Lambda e^- \nu$, the error quoted is dominated by statistical fluctuations in the $\Xi^- \rightarrow \Lambda e^- \nu$ events and in the background processes.

Our results for the branching ratios, after subtraction of our estimated background, are given in Table IV. Previous counter experiments have not separated $\Xi^- \rightarrow \Lambda e^- \nu$ from possible $\Xi^- \rightarrow \Sigma^0 e^- \nu$ events. The $\Sigma^0 e^- \nu$ mode is expected to be about $\frac{1}{8}$ of the $\Lambda e^- \nu$ mode (mostly from phase-space considerations). Our kinematic cuts remove about 90% of any $\Sigma^0 e^- \nu$ mode from our final sample, resulting in an estimated background from this process of about 1 event. ($\epsilon_\beta/\epsilon_n \sim 0.29$ for $\Xi^- \rightarrow \Lambda e^- \nu$, but would be ~0.1 for $\Xi^- \rightarrow \Sigma^0 e^- \nu$.)

Table IV also shows the Cabibbo predictions from recent fits.[10,11] For the $\Sigma^- \rightarrow \Lambda e^- \nu$ mode, we are in good agreement with the Cabibbo prediction and also in agreement with a compilation of recent experiments. For the $\Xi^- \rightarrow \Lambda e^- \nu$ decay, our value is somewhat below but consistent with both the Cabibbo theory prediction and previous experiments.

The Σ leptonic rate is

$$= \tfrac{2}{3} \cos^2(\theta_{\text{Cab}}) D^2 \rho \Gamma$$

in which ρ is the phase-space factor and Γ is the lifetime. We see that this depends only weakly on the Cabibbo angle (since $\Sigma^- \rightarrow \Lambda e^- \nu$ is a strangeness-conserving decay). Thus the agreement of our branching ratio implies agreement with the D value found in the Cabibbo fit, as well as the SU_3 assumptions of the theory.

The $\Xi^- \rightarrow \Lambda e^- \nu$ branching ratio, however, is sensitive to a combination of F, D, and Cabibbo angle, and the SU_3 structure:

$$= \tfrac{3}{2} \sin^2(\theta_{\text{Cab}}) [\rho_V + (F - D/3)^2 \rho_A] \Gamma$$

in which ρ_V and ρ_A are the phase-space factors. Thus, agreement or disagreement with the predicted value does not clearly test any single parameter but rather the general coherence and consistency of the theory and parameters.

TABLE IV. Branching-ratio results.

$\Sigma^- \rightarrow \Lambda e \nu$	No. of events [a]	$(\Sigma^- \rightarrow \Lambda e\nu)/(\Sigma^- \rightarrow n\pi^-)$
This experiment	119 (5)	$(0.63 \pm 0.11) \times 10^{-4}$
World	180 [b]	$(0.60 \pm 0.06) \times 10^{-4}$ [c]
Cabibbo		0.64×10^{-4} [d] 0.71×10^{-4} [e]
$\Xi^- \rightarrow \Lambda e\nu$	No. of events	$(\Xi^- \rightarrow \Lambda e\nu)/(\Xi^- \rightarrow \Lambda\pi^-)$
This experiment	14 (3.4)	$(0.30 \pm 0.13) \times 10^{-3}$
World		
$\Xi^- \rightarrow \Lambda e\nu$	5 [f]	$(0.7 \pm 0.3) \times 10^{-3}$ [c]
$\Xi^- \rightarrow \Lambda e\nu$, $\Sigma^0 e\nu$	23 (6) [g]	$(0.68 \pm 0.22) \times 10^{-3}$ [g]
Cabibbo		
$\Xi^- \rightarrow \Lambda e\nu$		0.49×10^{-3} [d] 0.46×10^{-3} [e]
$\Xi^- \rightarrow \Sigma^0 e\nu$		0.10×10^{-3} [d] 0.08×10^{-3} [e]

[a] Estimated background is in parentheses.
[b] References 17–20.
[c] Reference 6.
[d] Reference 10.
[e] Reference 11. [Preliminary branching ratios from this experiment (Ref. 31) were included as experimental input.]
[f] References 21–27.
[g] Reference 28.

B. g_V/g_A and g_{WM}/g_A for $\Sigma^- \rightarrow \Lambda e^- \nu$

In determining g_V/g_A for the $\Sigma^- \rightarrow \Lambda e^- \nu$ decay, we again depend upon the technique of generating fake events and following them through the analysis. This allows us to study distortions, spreading, and efficiency variations over the Dalitz plot.

A sample of fake $\Sigma^- \rightarrow \Lambda e^- \nu$ events was generated uniformly over the Dalitz plot and followed carefully through the analysis. Comparison of the final analysis (in the Ξ c.m.) values for T_Λ, T_e and $(\hat{p} \cdot \hat{\Lambda})$ with the initial unspread values yields estimates of distortions. We plot each fake event with a weight proportional to $|\text{decay matrix element}|^2$ evaluated with the unspread T_Λ, T_e, $(\hat{p} \cdot \hat{\Lambda})$ and a trial g_V/g_A. Normalizing the fake sample to the real data then allows us to compare our real data (having removed the two recognizable background events) to distributions expected for different form-factor ratios (g_V/g_A, g_{WM}/g_A ratios, in practice). The Dalitz plot is divided into six bins, and each bin is further subdivided into positive or negative Λ helicity. [To compare with previous analyses, we note that $\hat{p} \cdot \hat{\Lambda}$ in the Ξ c.m. $= -\hat{p} \cdot \hat{\Xi}$ in the Λ c.m. $= -\hat{p} \cdot \hat{k}$, where $\hat{k} = (\vec{e} + \vec{\nu})/|\vec{e} + \vec{\nu}|$ in the Λ c.m.] Using a χ^2 method, the population of these bins for the real data is then compared to the fake data with the fake data weighted according to the test matrix elements. Figure 16 shows the Dalitz-plot weighted contours expected for perfect efficiency for pure g_V, pure g_A, $g_A = -g_V$, and $g_V = 0$, $g_{WM} = 2g_A$ ($\approx$ the CVC prediction). Figure 17 shows the predicted helicity for different form factors. Figure 11(b) shows our expected efficiency over the Dalitz plot.

Tables V and VI summarize our results and compare them with previous results. Figure 18 shows the results of previous experiments,[3,7] together with our result and a 1-standard-deviation χ^2 contour as a function of g_{WM}/g_A and g_V/g_A. We find

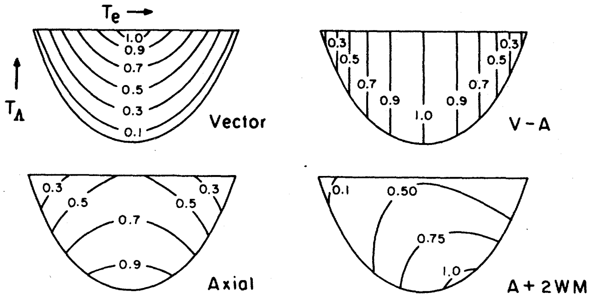

FIG. 16. Expected event-population contours over a Dalitz plot for $\Lambda e^- \nu$ final-state β decays, for representative form factors. The extent of the Dalitz plot (i.e., the energy scale) would vary from $\Sigma^- \rightarrow \Lambda e^- \nu$ to $\Xi^- \rightarrow \Lambda e^- \nu$, but the relative positions of contours within the plots would be similar.

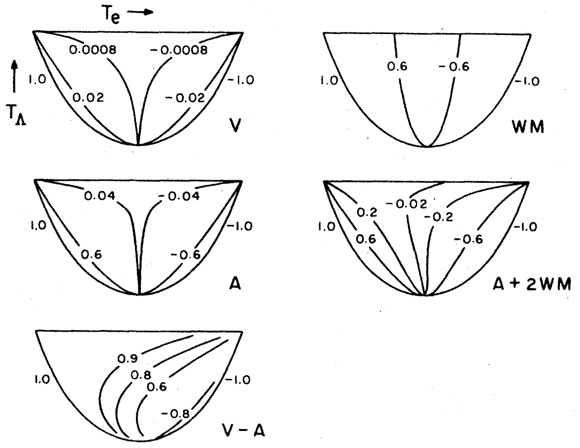

FIG. 17. Expected Λ-helicity contours over a Dalitz plot for $\Lambda e^- \nu$ final-state β decays, for representative form factors. The extent of the Dalitz plot (i.e., the energy scale) would vary from $\Sigma^- \to \Lambda e^- \nu$ to $\Xi^- \to \Lambda e^- \nu$, but the relative positions of contours within the plots would be similar.

$g_V/g_A = 0.32 \pm 0.30$ and $g_{WM}/g_A = 0.6 \pm 3.6$, with systematic errors approximately a third of the quoted errors. We have estimated our systematic errors by varying the binning of the data, and by noting that the fake-data sample used is ~20 times the real data, so that the statistical errors from the fake data are about a quarter of those for the real data. With $g_V = 0$ (CVC prediction) we find $g_{WM} \sim 0.75 \pm 3.5$, with $g_{WM} = 0$ we find $g_V/g_A = 0.32 \pm 0.25$, and with $g_{WM} = 1.7$ (CVC-SU$_3$ prediction) we find $g_V = 0.29 \pm 0.29$. As might be expected from the Dalitz plot and Λ helicity distribution variations with g_V, shown in Figs. 16 and 17, a large part of our discrimination for g_V/g_A comes from the Λ helicity information. (From the Dalitz plot alone $|g_V/g_A| = 0.5 \pm 0.5$.) Figure 19 is a plot of the helicity. The dashed line shows the result for the fake-data events, for a uniformly populated Dalitz plot with uniform Λ helicity distribution. The second dashed line shows the expected result for $g_{WM} = 0.6$, $g_V/g_A = 0.32$, our predicted result. This plot is insensitive to g_{WM} and shows the connection between our sign convention and measurement data. In our sign convention, the same as that of Refs. 3 and 4 but opposite to that of Refs. 6 and 7, g_V/g_A for the neutron is negative. One can also estimate g_V/g_A from this plot, neglecting efficiency variation over the Dalitz plot and using the predicted slope of the helicity plot from Ref. 2. Our result changes by approximately half of our quoted errors when we estimate g_V/g_A in this simple manner. Electron laboratory momentum, for low-momentum electrons, is highly correlated with position on the Dalitz plot, as is predicted Λ polarization (and therefore Λ helicity). Although such effects do not dominate in our experiment because of our small statistical sample and relatively uniform collection efficiency over the Dalitz plot, variations in Dalitz-plot efficiency could cause serious errors in interpretation of Dalitz plots or Λ helicity distributions if no corrections were made. Such effects will be of more importance in next generation high-statistics experiments.

TABLE V. g_V/g_A in $\Sigma^- \to \Lambda e^- \nu$.

Assumed $\frac{g_{WM}}{g_A}$ condition	Ref. 3 (186 events) Σ^+ and Σ^-	Ref. 7 (55 events) Σ^- only	This experiment (119 events) Σ^- only
0	-0.37 ± 0.20	0.25 ± 0.35	0.32 ± 0.25
1.7	-0.45 ± 0.20	0.17 ± 0.35	0.29 ± 0.29
Correlated with g_V/g_A	-0.64 ± 0.67		0.32 ± 0.30

It has previously been suggested[32] that an estimate of g_{WM} in Σ leptonic decay would yield an estimate of $\mu_{\Sigma\Lambda}$ through CVC arguments, and $\mu_{\Sigma\Lambda}$ is in turn related to the Σ^0 lifetime. However, recently the Σ^0 lifetime has been measured by Coulomb production of Σ^0 in the CERN neutral-hyperon beam,[33] yielding a 10% measurement of $\mu_{\Sigma\Lambda}$, in agreement with the SU$_3$ prediction. Thus the usefulness of the g_{WM} measurement in $\Sigma^- \to \Lambda e^- \nu$ is for the sake of understanding the weak interactions, rather than as a measurement of the Σ^0 lifetime.

TABLE VI. g_{WM}/g_A in $\Sigma^- \to \Lambda e^- \nu$.

Condition on g_V/g_A	Ref. 3 (186 events) Σ^+ and Σ^-	Ref. 7 (55 events) Σ^- only	This experiment (119 events) Σ^- only
0	2.4 ± 2.1	3.5 ± 4.5	1.75 ± 3.5
Correlated with g_{WM}/g_A	$5.8^{+4.9}_{-3.8}$		0.6 ± 3.6

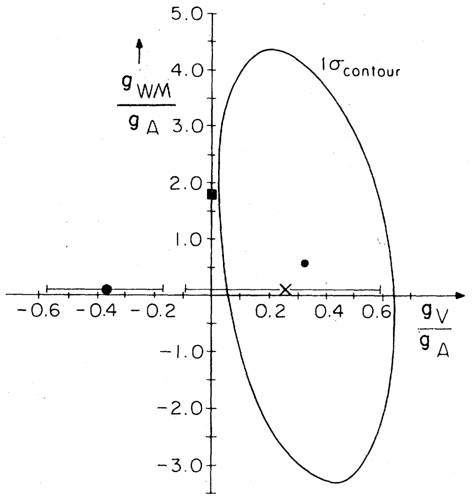

FIG. 18. χ^2 contours for g_V/g_A and g_{WM}/g_A for the 119 final $\Sigma^- \rightarrow \Lambda e^- \nu$ candidate sample. The center of the ellipse ($g_V/g_A = 0.32$, $g_{WM}/g_A = 0.6$) gives our reported values for the form factors. The ellipse contour indicates an increase of the χ^2 by one, corresponding to our reported error. Results of previous measurements for the g_V/g_A are plotted with our sign convention (see text), assuming $g_{WM} = 0$, for comparison. The ● shows the result of Ref. 3, the **×** shows the result of Ref. 7; and the ■ is the Cabibbo prediction.

Tables V and VI compare our final g_V/g_A and g_{WM}/g_A measurement to other published measurements. The average of all the measurements is in agreement with Cabibbo predictions. More simply, without efficiency variations over the Dalitz plot, but simply looking at distributions of

$$\alpha = \hat{p} \cdot \hat{P}^+ \ , \ \Lambda_{\text{helicity}}, \text{ or } \beta = \hat{p} \cdot \hat{P}^-$$

[where $\hat{P}^{\pm} = (\vec{p}_e \pm \vec{p}_\nu)/|\vec{p}_e \pm \vec{p}_\nu|$ in the Λ c.m.], we find $g_V/g_A = 0.01 \pm 0.3$, 0.17 ± 0.35, or 0.8 ± 0.95, respectively.

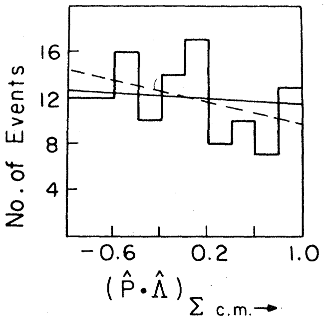

FIG. 19. A plot of Λ helicity in the Σ^- center of mass is shown, integrated over the Dalitz plot. The solid line indicates the small instrumental bias which would be observed if the asymmetry were zero and the Dalitz plot were uniform. The dashed line is for $g_V/g_A = 0.32$, $g_{WM} = 0.6$, our reported values. However, the plot is insensitive to g_{WM}/g_A, and the shape of the line with g_V/g_A positive (depletion of events with positive helicity) unambiguously demonstrates our sign convention.

In our complete Dalitz-plot Λ-helicity analysis we have used the results of Ref. 4 (in terms of event distribution and Λ helicity over the Dalitz plot) with corrections as noted in our appendix. Nonrelativistically, Λ helicity is an average of α and β above. And, indeed, we see that an average of the α and β results above would be consistent with our Λ-helicity result. These simple methods are sufficient to check the approximate value of g_V/g_A.

To evaluate $\text{Im}(g_V/g_A)$, we looked at a plot of $\gamma = \hat{p} \cdot \hat{P}$, where $\hat{P} = (\vec{p}_e \times \vec{p}_\nu)|\vec{p}_e \times \vec{p}_\nu|$, ignoring efficiency variations over the Dalitz plot, and find the asymmetry in the distribution to be 0.08 ± 0.16. Using the results from Ref. 2, we estimate $\text{Im}\, g_V/g_A = -0.2 \pm 0.7$.

C. Search for $\Xi^- \rightarrow \Sigma^0 e^- \nu$

The candidates selected by the $\Lambda\pi^-$ mass cut and the $\check{C}E$ timing cut were examined to search for decays of the type $\Xi^- \rightarrow \Sigma^0 e^- \nu$, $\Sigma^0 \rightarrow \Lambda\gamma$. Our Monte Carlo program was used to calculate the mass distribution for the $\Lambda e^- \nu$ system, calculated as for the selection of β-decay candidates. From this distribution, we found that the cut $1.24 < M_{\Lambda e^- \nu} < 1.36$ GeV/c^2, while eliminating most of the $\Sigma^- \rightarrow \Lambda e^- \nu$ candidates, would retain 87% of the $\Xi^- \rightarrow \Sigma^0 e^- \nu$ sample. For events satisfying this mass cut, we made the further restriction that the reconstructed events be compatible kinematically with the γ ray from the Σ^0 decay entering our γ detector, including the effect of our kinematic and geometrical resolution. The sample remaining after these cuts consisted of 67 candidates. For these events we examined the photographs of the steel-plate spark chamber. Before searching for γ rays in this sample, studies were made of the photographs from test data taken, in which a neutral final state was demanded in the trigger. These test data thus contain a large number of π^0's. A sample of well reconstructed $\Xi^- \rightarrow \Lambda\pi$ events were also studied. These studies led us to adopt the following criteria for the identification of γ-ray showers. (A) A narrow shower is visible in the chamber, starting with at least three single sparks, (B) the object which initiates the shower is neutral at its entry into the detector, and (C) the shower does not appear to come from any hadronic interaction from the region of the decay fiducial volume. With these criteria, about 1% of the reconstructed $\Lambda \rightarrow p\pi^-$ sample contained an apparent γ ray, which serves to give us an estimate of the background expected in the $\Sigma^0 e^- \nu$ sample.

The total sample of 10^6 triggers in the experiment contained only about 7×10^5 photographs, due to inefficiencies in the operation of the optical system. For our particular sample of 67 candidates, photographs exist for only 45 of them. In order to check the correspondence between the photograph and the event on magnetic tape, these photographs were carefully examined for consistency with the charged tracks found by the pattern-recognition program. Three photographs failed this consistency test and were therefore considered to be events for which photographs do not exist. For the remaining 42 events with photographs, 18 were very clean events with no hadronic interactions in the steel-plate chamber. One of these contained a clear γ-ray shower. Eighteen photographs contain hadronic interactions, but in only a small region of the detector would the detection of a γ-ray shower be difficult. Six of the photographs contain complicated hadronic interactions, in which the identification of a γ-ray would be difficult over as much as half of the area of the detector. In these 24 photographs containing hadronic interactions, no γ rays were found which satisfy the above criteria. If we assume that the γ-ray efficiency of the detector is given by the fraction of the cross-sectional area which is free of charged tracks, we obtain an average efficiency of ~88%.

The single event containing a γ ray was measured and, from the conversion point of the γ and the decay vertex, the angles of the Σ^0 were found. By assuming the mass of the Σ^0, we used the reconstructed Λ momentum vector to obtain the Σ^0 momentum. As for the $\Xi^- \to \Lambda e^- \nu$ decay, we assume the mass of the parent particle to be the Ξ and calculate M_ν^2. For this event we obtain $M_\nu^2 = 0.009\ \text{GeV}^2$, whereas our criterion for acceptance for the other decay modes is $M_\nu^2 = 0.004\ \text{GeV}^2$. Thus we conclude that the event is excluded kinematically and is a background event. As a check on this calculation and to test our sensitivity to the measurement of the γ-ray coordinates, we have calculated the locus of points in the detector at which the γ ray would have to convert to be accepted as a good event. We find that the locus which corresponds to $M_\nu^2 = 0.004\ \text{GeV}^2$ is at least 60 cm from the measured conversion point, which substantiates our conclusion that the event is due to a background process. One background event in 42 candidates is not unreasonable, as we have determined the background level to be about 1% from the $\Lambda\pi$ sample mentioned above.

Therefore, in a sample of 42 events with photographs, we find no candidates for $\Xi^- \to \Sigma^0 e^- \nu$. An upper limit to the branching ratio can be calculated using the acceptance calculated from our Monte Carlo program (27% relative to $\Xi^- \to \Lambda\pi$), the $\check{C}E$ efficiency (90%), the γ-ray detector efficiency (88%), and the effective number of reconstructed $\Xi \to \Lambda\pi$, which for this sample with photographs is 7.6×10^4. From these quantities we obtain

$$(\Xi^- \to \Sigma^0 e^- \nu)/(\Xi^- \to \Lambda\pi^-) < 1.4\times 10^{-4}\ (90\%\ \text{C.L.}).$$

This value is consistent with the prediction of the Cabibbo theory and is a factor of 3.6 lower than the previously published upper limit[27] for this branching ratio.

D. $\Xi^- \to \Lambda\mu^-\nu$ search and limits

Since we have a large sample of reconstructed $\Xi^- \to \Lambda\pi^-$ from "Ξ" triggers (no Čerenkov requirement), we have also searched for the decay $\Xi^- \to \Lambda\mu^-\nu$. From Cabibbo theory, it should have the same form for the decay matrix as $\Xi^- \to \Lambda e^- \nu$, but a lower rate, since the available phase space is less for the $\Lambda\mu^-\nu$ final state than for the $\Lambda e^-\nu$ final state. There is one recognized example of $\Xi^- \to \Lambda\mu^-\nu$ (Ref. 27) for a measured branching ratio of $(3.5 \pm 3.5)\times 10^{-4}$, comparable to our measured $\Xi^- \to \Lambda e^- \nu$ rate. Thus a search for $\Xi^- \to \Lambda\mu\nu$ is interesting, either to confirm a high rate, or to increase the denominator of searched $\Xi^- \to \Lambda\pi^-$ and thus reduce the effective rate.[27] For this search we have no help from the $\check{C}E$ counter, since the μ does not fire $\check{C}E$. Thus the separation must be done entirely by kinematic cuts, and we chose to use only events from "Ξ" triggers (no $\check{C}E$ required). As for the other β-decay studies discussed in this paper, we used only the cleaner part of our running (data from run B and run C, ≈8180 reconstructed $\Xi^- \to \Lambda\pi^-$ events). The cuts we have chosen to separate $\Xi^- \to \Lambda\mu^-\nu$ from the normal $\Lambda\pi^-$ mode are the following.

(1) $|M_{\Lambda\pi} - 1.321| > 0.020\ \text{GeV}/c^2$. [This removes only ~29% of the $\Lambda\mu^-\nu$ events but as discussed in the $\Lambda e^-\nu$ section, removes ~97% of the normal $\Lambda\pi^-$ decay (133 candidates remain].

(2) $1.27 < M_{\Lambda\mu\nu} < 1.36\ \text{GeV}/c^2$ (centered at 1.321 for $\Xi^- \to \Lambda\mu^-\nu$). This is a generous cut, removing only ~$\frac{1}{6}$ of the remaining events but effective against $\Lambda\pi^-$ background (33 candidates remain after this cut).

(3) Mass of $(\Xi - \Lambda)^2 > 0.030\ \text{GeV}/c^2$. [Note this should be centered around $M\pi^2$, ~0.020 (GeV/c^2) for $\Xi^- \to \Lambda\pi^-$ events.] A graph for the real data, indicating our resolution and the effect of the cut on the $\Lambda\mu^-\nu$ mode, is shown in Fig. 20. About 45% of the remaining $\Xi^- \to \Lambda\mu^-\nu$ sample are removed by this cut.

(4) "T_π": Kinetic energy of negative track, interpreted as a pion in the Ξ^- cm $< 0.020\ \text{GeV}/c^2$.

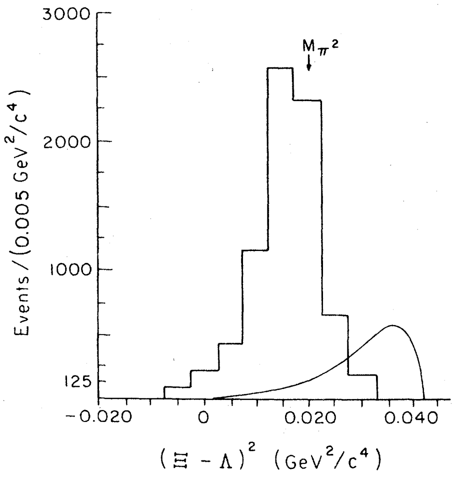

FIG. 20. The (missing mass)^2, $(\Xi - \Lambda)^2$. For the real data, predominantly $\Xi^- \to \Lambda\pi^-$, this distribution peaks at $M_\pi{}^2$, as shown. For the $\Xi^- \to \Lambda\mu^-\nu$ events, the predicted distribution is broad and is shown by the solid curve, with arbitrary normalization.

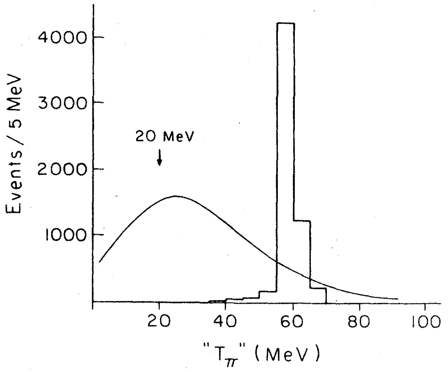

FIG. 21. "T_π" for the event topology $\Xi^- \to \Lambda X^-$. "T_π" is the kinetic energy, in the Ξ^- center of mass, of x^- interpreted as a pion. For the real data, predominantly $\Xi^- \to \Lambda\pi^-$, this distribution is sharply peaked at the value for the usual two-body $\Lambda\pi^-$ decay mode, ~ 58 MeV. For the entire sample of 8180 $\Xi^- \to \Lambda\pi^-$ plotted in this figure, 11 have "T_π" less than 20 MeV, the cut used in searching for the $\Xi^- \to \Lambda\mu^-\nu$.

This distribution should be centered at about 0.057 GeV/c^2 for $\Xi \to \Lambda\pi$ events. A graph for our $\Xi^- \to \Lambda\pi^-$ events and predictions for the $\Lambda\mu^-\nu$ events are shown in Fig. 21. This cut removes ~70% of the remaining $\Lambda\mu^-\nu$ events. It is a heavy cut but effectively removes the $\Xi^- \to \Lambda\pi^-$ contamination.

Only 12.4% of $\Xi^- \to \Lambda\mu^-\nu$ Monte Carlo events which occurred in our fiducial volume remain after these cuts, reducing our effective denominator to 0.124×8180 or ≈ 1077 events. When the same cuts were applied to our 8180 reconstructed clean $\Xi^- \to \Lambda\pi^-$ events, no events survived. If we see no events, by Poisson statistics, at the 90% confidence level, 2.3 might have been the mean. Thus our branching ratio would be $< 2.3 \times 10^{-3}$ (branching ratio from our data alone, 90% C.L.). This is not very useful. However, combining our sample with that of Ref. 27 we find 1 event in an effective sample of 2835 (Ref. 27) + 1017 (our experiment) for a branching ratio of $(2.6 \pm 2.6) \times 10^{-4}$, somewhat smaller, as expected, than the previous branching ratio of $(3.5 \pm 3.5) \times 10^{-4}$.

ACKNOWLEDGMENTS

We wish to thank R. Prepost at the University of Wisconsin for the loan of the optical spark chamber and the optical system. We also acknowledge the assistance provided us by the Carnegie-Mellon University bubble chamber group in the scanning and measuring of the spark-chamber film. We acknowledge the assistance provided by the staff of the Brookhaven National Laboratory and the assistance provided in data analysis by R. Kroll. D. Groff assisted in the scanning for $\Xi^- \to \Sigma^0 e^-\nu$ events, and the $\Xi^- \to \Lambda\bar{\mu}\nu$ branching ratio was the result of an undergraduate project undertaken by Mr. Groff. One of us (J.T.) wishes to acknowledge helpful conversations with R. Willey and L. Wolfenstein. This research was supported in part by the National Science Foundation and the U. S. Department of Energy.

APPENDIX

We follow the notation and formulas of Ref. 4, keeping only vector (g_V), tensor (g_{WM}), and axial-vector (g_A) terms. We collect the formulas used, both for convenience and to correct some errors in the appendix of Ref. 4. The current matrix element is written as

$$\langle B | J^\mu(0) | A \rangle = \left(\frac{m_A m_B}{E_A E_B}\right)^{1/2} \bar{u}_B \left[g_V \gamma_\mu + \frac{g_{\mathrm{WM}}}{m_A} \sigma_{\mu\nu} k_\nu + g_A \gamma_\mu \gamma_5 \right] u_A \,.$$

With the definitions

$$F_1 = g_V + \left(1 + \frac{m_B}{m_A}\right) g_{\mathrm{WM}} \,,$$

$$F_2 = -2\, g_{\mathrm{WM}}\,,$$

$$G_1 = g_A\,,$$

one finds

$$\begin{aligned}
\mathrm{I} = {} & \frac{(2\pi)^3}{|G|^2}\,\frac{d^2\Gamma(E_l,E_B)}{dE_l\,dE_B} \\
= {} & 2|F_1|^2\{-2m_AE_l^2+E_l[-2m_AE_B+2m_A^2+m_l^2]+[-m_AE_B^2+E_B(m_A^2+m+m_Bm_A)+(-mm_A+m_Bm_1)]\} \\
& +2|G_1|^2\{-2m_AE_l^2+E_l[-2m_AE_B+(2m_A^2+m_1^2)]+[-m_AE_B^2+E_B(m_A^2+m-m_Bm_A)+(-mm_A-m_Bm_1)]\} \\
& +|F_2|^2\{E_l^2(-2E_B-2m_B)+2E_l[-E_B^2+(m_A-m_B)E_B+m_Am_B]+[m_AE_B^2+E_B(m_1+m_Am_B)+m_Bm_1]\} \\
& +2\,\mathrm{Re}\,F_1F_2^*\{2E_l^2(-m_B-m_A)+E_l[2E_B(-m_B-m_A)+(2m_Bm_A+2m_A^2+m_l^2)] \\
& \qquad +E_B(m_A^2+m_l^2+m_Am_B)+(m_Bm_1-m_Am)\} \\
& +4\,\mathrm{Re}\,F_1G_1^*\{E_l[m_A^2+m_B^2-2m_AE_B]+[-E_B^2m_A+E_B(m+m_A^2)-m_Am]\}\,,
\end{aligned}$$

where $m=\frac{1}{2}\,(m_A^2+m_B^2+m_l^2)$, $m_1=-m+m_l^2$, $m_2=m-m_B^2$.

To find the predicted Λ helicity, $\Lambda_{\mathrm{hel}}=\mathrm{II}/(0.5\times\mathrm{I})$, where I is the expression above and

$$\begin{aligned}
\mathrm{II} = {} & (|M(\vec{\mathrm{s}})|^2-|M(-\vec{\mathrm{s}})|^2)\,\frac{(2\pi)^3}{2|G|^2}\bigg|_{\vec{\mathrm{s}}\cdot\hat{p}_B=1} \\
= {} & \frac{|F_1|^2}{P_B}\,(E_l\{2m_AE_B^2+E_B(-m_B^2-m_A^2-2m_Am_B)+m_B(m_A^2+m_B^2)] \\
& \qquad +\{E_B^3m_A+E_B^2(-m-m_A^2-m_Am_B)+E_B[m_Am+m_B(m+m_A^2)]-m_Am_Bm\}) \\
& +\frac{|G_1|^2}{P_B}\,(E_l[2m_AE_B^2+E_B(-m_B^2-m_A^2+2m_Am_B)-m_B(m_A^2+m_B^2)] \\
& \qquad +\{E_B^3m_A+E_B^2(-m-m_A^2+m_Am_B)+E_B[m_Am+m_B(-m-m_A^2)]+m_Amm_B\}) \\
& -2\,\mathrm{Re}\,\frac{F_1G_1^*}{P_B}\{E_l^2(-2m_AE_B+2m_B^2)+E_l[-2m_AE_B^2+E_B(m_2+m+m_A^2+2m_B^2)-2m_B^2m_A] \\
& \qquad +[-m_AE_B^3+E_B^2(m+m_A^2)-m_AmE_B]\} \\
& +\mathrm{Re}\,\frac{G_1F_2^*}{P_B}\,(E_l^2[2E_B(-m_B+m_A)+2m_B(m_A-m_B)] \\
& \qquad +E_l\{2E_B^2(m_A-m_B)+E_B[4m_Am_B-(2m+m_A^2+m_B^2)]+m_B(m_B^2-2m-m_A^2+2m_Am_B)\} \\
& \qquad +[E_B^2(m_Am_B-m_A^2-m_l^2)+E_B(m_A-m_B)(m-m_Am_B)+m_B(m_Am+m_Bm_1)])\,.
\end{aligned}$$

---

*Present address: Physics Department, University of Pennsylvania, Philadelphia, Pa. 19104.

†Present address: Singer Company, Kearfott Division, 150 Totowa Road, Wayne, New Jersey 07470.

[1] W. E. Cleland *et al.*, preceding paper, Phys. Rev. D 21, 12 (1980).

[2] W. Alles, Nuovo Cimento 26, 1429 (1962).

[3] P. Franzini *et al.*, Phys. Rev. D 6, 2417 (1972).

[4] W. Willis and J. Thompson, in *Advances in Particle Physics*, edited by R. L. Cool and R. E. Marshak (Wiley, New York, 1968), Vol. I, p. 458.

[5] N. Cabibbo and P. Franzini, Phys. Lett. 3, 217 (1963).

[6] Particle Data Group, Phys. Lett. 75B, 1 (1978); Rev. Mod. Phys. 48, S1 (1976).

[7] W. Tanenbaum *et al.*, Phys. Rev. D 12, 1871 (1975). (This experiment reconstructed $\Xi^-\to\Lambda e\nu$ with spark chambers, but did not report a branching ratio.)

[8] N. Cabibbo, Phys. Rev. Lett. 10, 531 (1963); N. Cabibbo and R. Gatto, Nuovo Cimento 15, 159 (1960).

[9] F. Wilczek and A. Zee, Phys. Rev. Lett. 42, 421 (1979).

[10] M. Roos *et al.*, Nucl. Phys. B77, 420 (1974) (renor-

malized values). See also H. Ebenhoh *et al.*, Z. Phys. 241, 473 (1971).

[11] R. E. Schrock and L. L. Wang, Phys. Rev. Lett. 41, 1692 (1978).

[12] M. M. Nieto, Rev. Mod. Phys. 40, 140 (1968).

[13] L. Gasiorowicz, *Elementary Particle Physics* (Wiley, New York, 1966).

[14] R. Willey (private communication).

[15] L. Wolfenstein, Phys. Rev. D 13, 3144 (1976).

[16] I. Bender, V. Linke, and H. J. Rothe, Institut für Hochenergiephysik der Universität Heidelberg report (unpublished).

[17] H. Courant *et al.*, Phys. Rev. 136, B1791 (1964).

[18] N. Barash *et al.*, Phys. Rev. Lett. 19, 181 (1967).

[19] F. Eisele *et al.*, Z. Phys. 221, 1 (1969).

[20] C. Baltay *et al.*, Phys. Rev. Lett. 22, 615 (1969).

[21] L. Jauneau *et al.*, Phys. Lett. 5, 261 (1963).

[22] J. P. Berge *et al.*, Phys. Rev. 147, 945 (1966).

[23] G. W. London *et al.*, Phys. Rev. 143, 1034 (1966).

[24] D. D. Carmony and G. M. Pjerrou, Phys. Rev. Lett. 10, 381 (1963).

[25] T. Trippe, 1967 (private communication), reported in Particle Data Group, Rev. Mod. Phys. 48, S1 (1976).

[26] J. R. Hubbard *et al.*, Phys. Rev. Lett. 20, 465 (1968).

[27] N. Yeh *et al.*, Phys. Rev. D 10, 3545 (1974).

[28] J. Duclos *et al.*, Nucl. Phys. B32, 493 (1971). (This experiment reported 21 events, $\Xi^- \rightarrow \Lambda e^- \nu + \Xi^- \rightarrow \Sigma^0 e\nu$.)

[29] George Cassiday, private communication.

[30] D. Underwood *et al.*, Phys. Rev. D 11, 2345 (1975).

[31] M. L. Herbert *et al.*, Phys. Rev. Lett. 40, 1230 (1978).

[32] A. D. Dolgov and V. I. Zakhorov, Phys. Lett. 48B, 43 (1974).

[33] F. Dydak *et al.*, Nucl. Phys. B118, 1 (1977).